Supplement of Earth Syst. Sci. Data, 18, 6763–6781, 2026
https://doi.org/10.5194/essd-18-6763-2026-supplement

Supplement of

TPHH: a long-term (1901–2023) high-resolution (1/30°) near-surface humidity dataset for the Tibetan Plateau generated via spatial downscaling based on hybrid-structure deep learning

Zheng Jin et al.

Correspondence to: Zezhou Chen (chenzz51@chinaunicom.cn), Zhaoxiang Liu (liuzx178@chinaunicom.cn), and Shiguo Lian (liansg@chinaunicom.cn)

Introduction

These supplementary materials provide the experimental setup and hyperparameters (**Table S1**); A summary of the 9-fold performance metrics of TPHH (**Table S2**); monthly validation results for 2 m temperature, 2 m specific humidity, and surface pressure (**Figures S1–S3**), together with long-term interannual series (**Figures S4–S6**) and comparisons with two representative datasets (**Figures S7**); the distribution of 41 tree-ring proxy groups and seasonal-window sensitivity results using AMJ, MJJ, and JJA specific humidity (**Figures S8–S23**); DEM ablation experiment results for the three variables during 1979–2008 and 1994–2023 (**Figures S24–S29**); Pettitt breakpoint detection patterns (**Figures S30–S32**); and monthly trend maps for temperature, specific humidity, and surface pressure across five 30-year periods (**Figures S33–S47**).

Table S1. Summary of experimental setup and hyperparameters.

Category	Parameter	Value / Setting
Hardware & System	GPU	NVIDIA H100 (80GB HBM3) × 8
	CPU	Intel(R) Xeon(R) Platinum 8468 (192 Cores)
	System Memory (RAM)	2.0 TiB
	Operating System	Ubuntu 22.04.5 LTS
Software Environment	Programming Language	Python 3.11.8
	Deep Learning Framework	PyTorch 2.6.0
	CUDA Compute Platform	CUDA 12.4
Model Architecture	Backbone	AFNONet (FourCastNet-based)
	Block Type	FFT
	Patch Size	8 × 8
	Hidden Dimension / Layers	768 / 12
	FNO Blocks	4
Training Config	Optimizer	AdamW, betas = (0.9, 0.95)
	Base Learning Rate	5e-4
	Learning Rate Scheduler	Cosine
	Global Batch Size	32 (via Data Parallel)
	Loss Function	MSELoss
	Total Epochs	100 (Fine-tuning disabled)
	Ensemble Strategy	9-fold Cross-Validation
Data & Grid Specs	Spatial Resolution	1/30° (~3 km)
	Grid Dimensions (H × W)	464 × 1008
	Input Variables	10 CRU variables
	Output Variables	temp, shum, pres

Table S2. Summary of the 9-fold performance metrics of TPHH. The units for temperature, specific humidity, and pressure are °C, g/kg, and hPa, respectively.

Variable	Fold groups	RMSE	R^2	MAE	IOA
Temperature	Fold 1	1.02	0.988	0.742	0.997
	Fold 2	0.990	0.989	0.705	0.997
	Fold 3	0.947	0.989	0.684	0.997
	Fold 4	0.957	0.989	0.694	0.997
	Fold 5	0.937	0.989	0.667	0.997
	Fold 6	0.985	0.989	0.699	0.997
	Fold 7	1.04	0.987	0.750	0.996
	Fold 8	0.962	0.989	0.693	0.997
	Fold 9	0.956	0.990	0.688	0.997
Specific humidity	Fold 1	0.300	0.991	0.217	0.997
	Fold 2	0.303	0.990	0.220	0.997
	Fold 3	0.295	0.991	0.210	0.997
	Fold 4	0.304	0.991	0.220	0.997
	Fold 5	0.281	0.991	0.202	0.997
	Fold 6	0.302	0.991	0.220	0.997
	Fold 7	0.301	0.991	0.219	0.997
	Fold 8	0.283	0.992	0.204	0.998
	Fold 9	0.287	0.992	0.211	0.997
Pressure	Fold 1	1.47	0.999	1.08	0.999
	Fold 2	1.46	0.999	1.08	0.999
	Fold 3	1.47	0.999	1.08	0.999
	Fold 4	1.51	0.999	1.11	0.999
	Fold 5	1.43	0.999	1.05	0.999
	Fold 6	1.49	0.999	1.08	0.999
	Fold 7	1.47	0.999	1.08	0.999
	Fold 8	1.40	0.999	1.02	0.999
	Fold 9	1.41	0.999	1.03	0.999

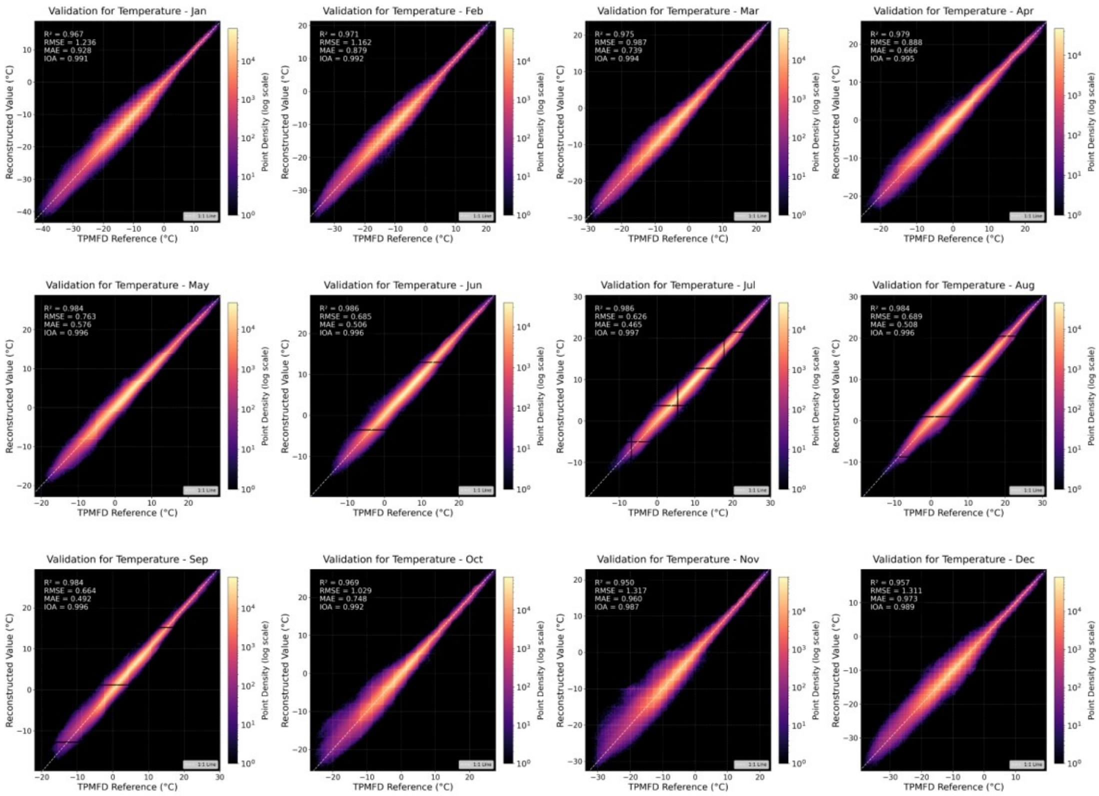

Figure S1. Monthly validation of the downscaled 2 m temperature (Temp). Density scatter plots comparing the TPHH reconstructed high-resolution temperature values against the TPMFD reference data across all 12 months. The dashed line represents the 1:1 reference line of perfect agreement. Color gradients indicate point density (logarithmic scale), with warmer colors representing higher concentrations of data points. Statistical metrics including the coefficient of determination (R^2), Root Mean Square Error (RMSE), Mean Absolute Error (MAE), and Index of Agreement (IOA) for each specific month are inset in the upper-left corner of the respective panels.

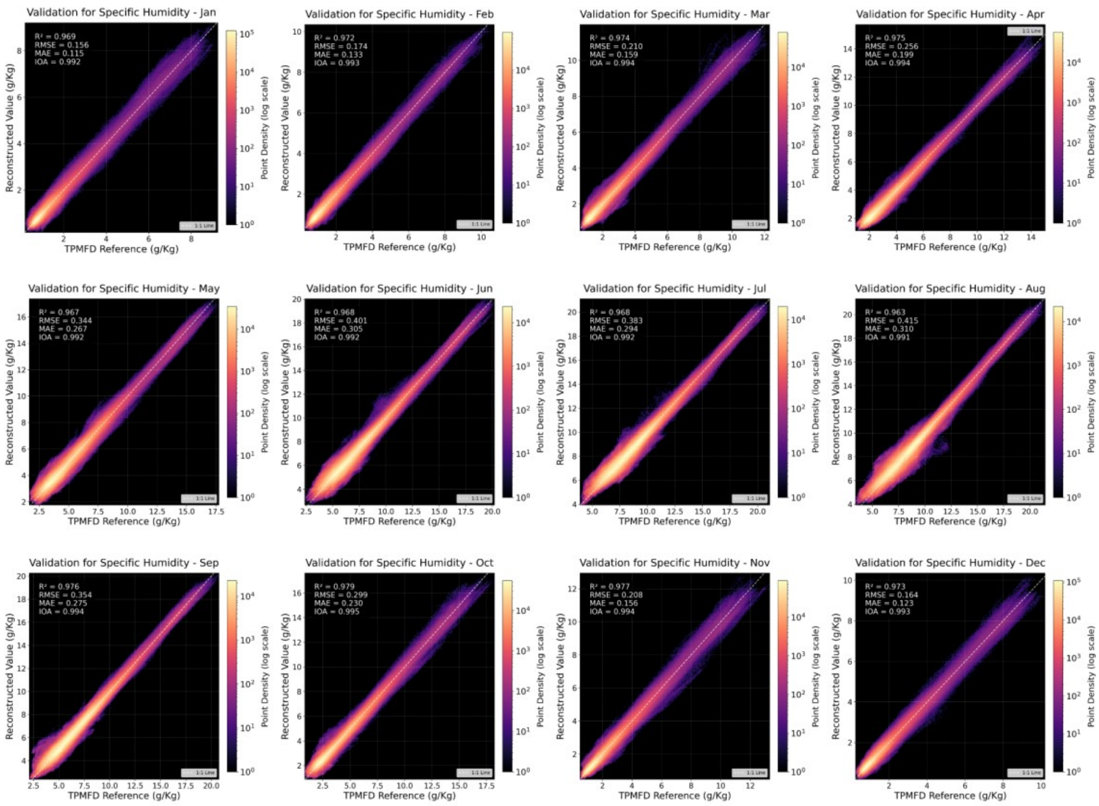

Figure S2. Monthly validation of the downscaled specific humidity (Shum). Density scatter plots comparing the TPHH reconstructed high-resolution specific humidity values against the TPMFD reference data across all 12 months. The dashed line represents the 1:1 perfect agreement line. Point density is mapped to the color gradient on a logarithmic scale. Inset evaluation metrics (R^2, RMSE, MAE, and IOA) quantify the model's monthly performance.

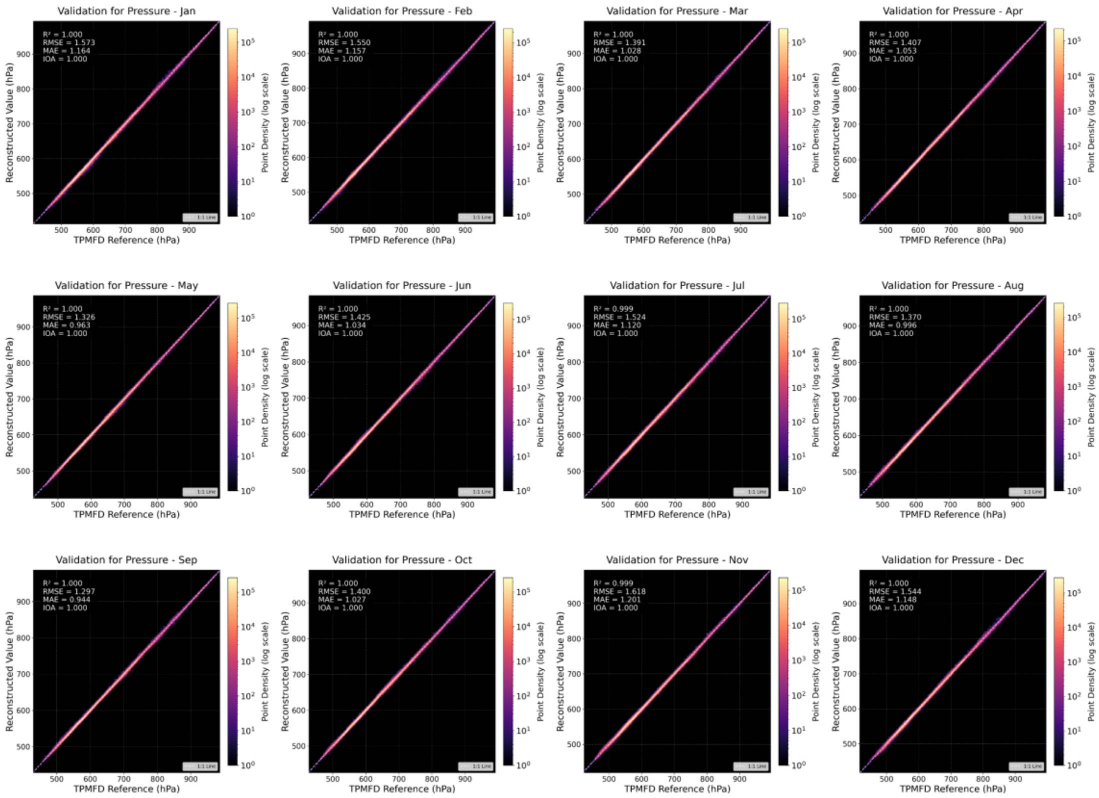

Figure S3. Monthly validation of the downscaled surface pressure (Pres). Density scatter plots showing the correlation between the TPHH reconstructed high-resolution surface pressure and the corresponding TPMFD reference data for each month. The 1:1 reference line is indicated by the dashed line. The color bar reflects the point density distribution (logarithmic scale). Quantitative metrics (R^2, RMSE, MAE, and IOA) derived from the masked evaluation over the Tibetan Plateau are provided in the upper-left corners.

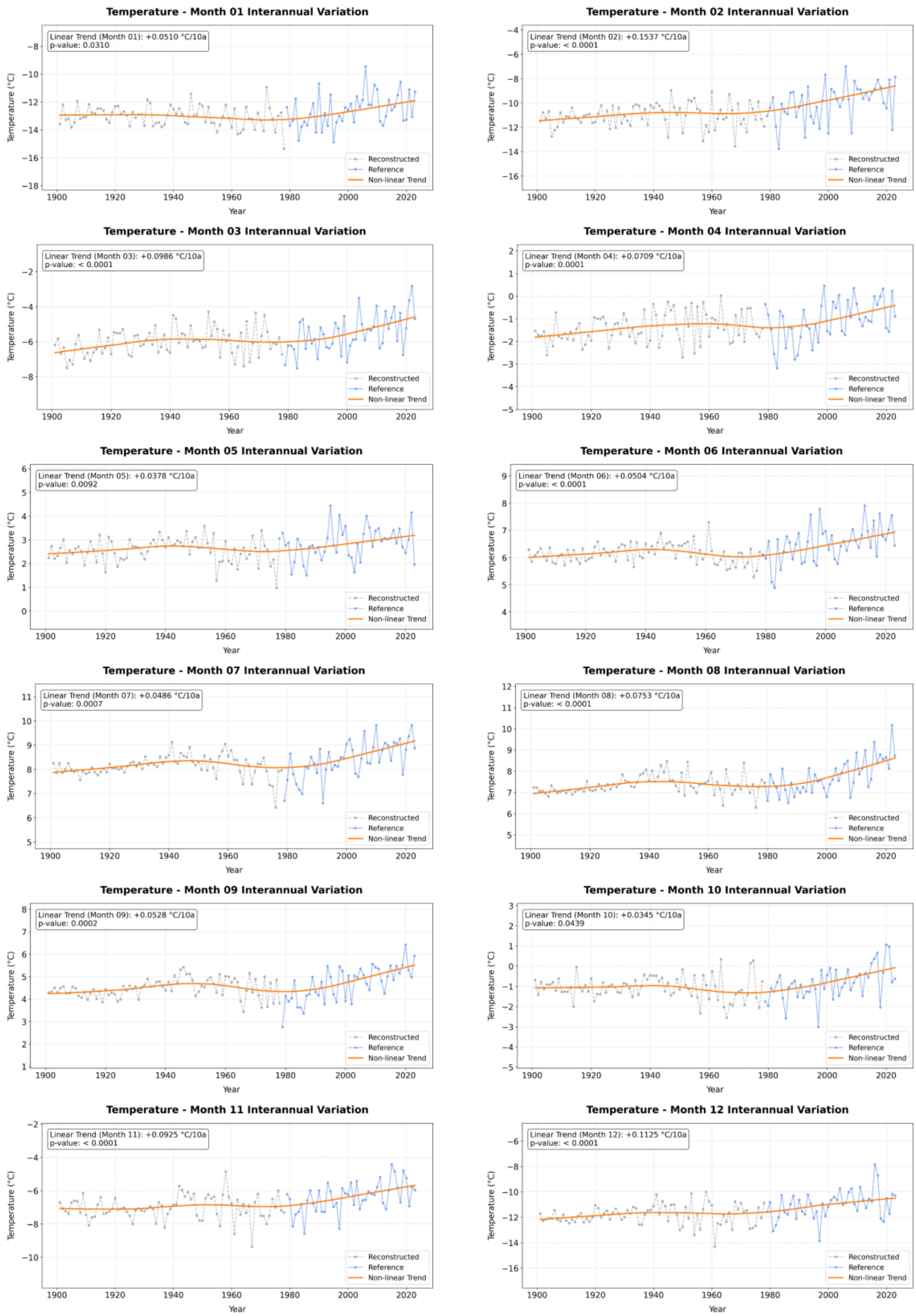

Figure S4. Monthly interannual variations of 2 m temperature over the Tibetan Plateau (1901–2023). Grey dashed and solid blue lines denote the reconstructed (1901–1978) and reference (1979–2023) data, respectively. The orange curve indicates the trend.

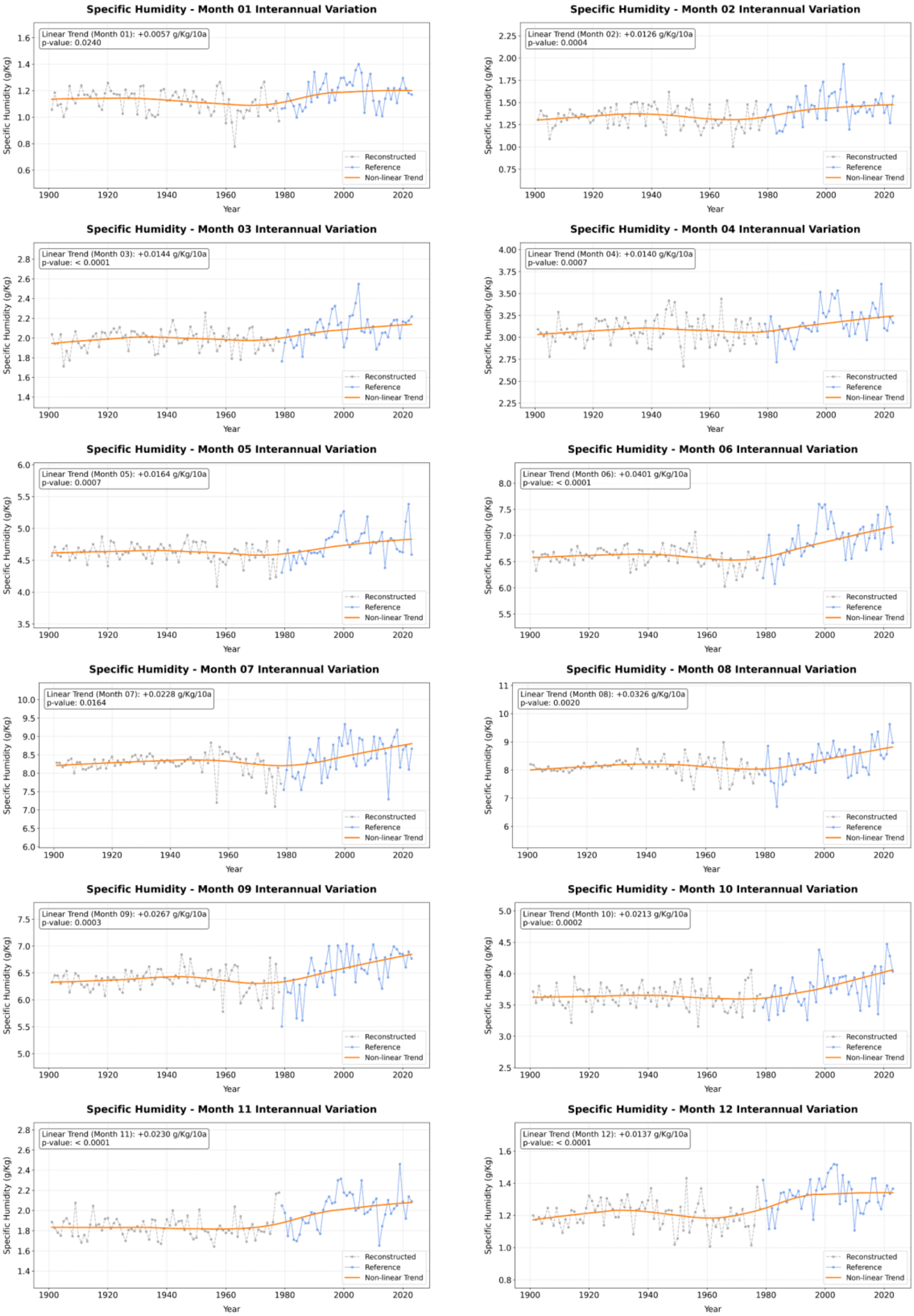

Figure S5. Monthly interannual variations of 2 m specific humidity over the Tibetan Plateau (1901–2023). Grey dashed and solid blue lines denote the reconstructed (1901–1978) and reference (1979–2023) data, respectively. The orange curve indicates the trend.

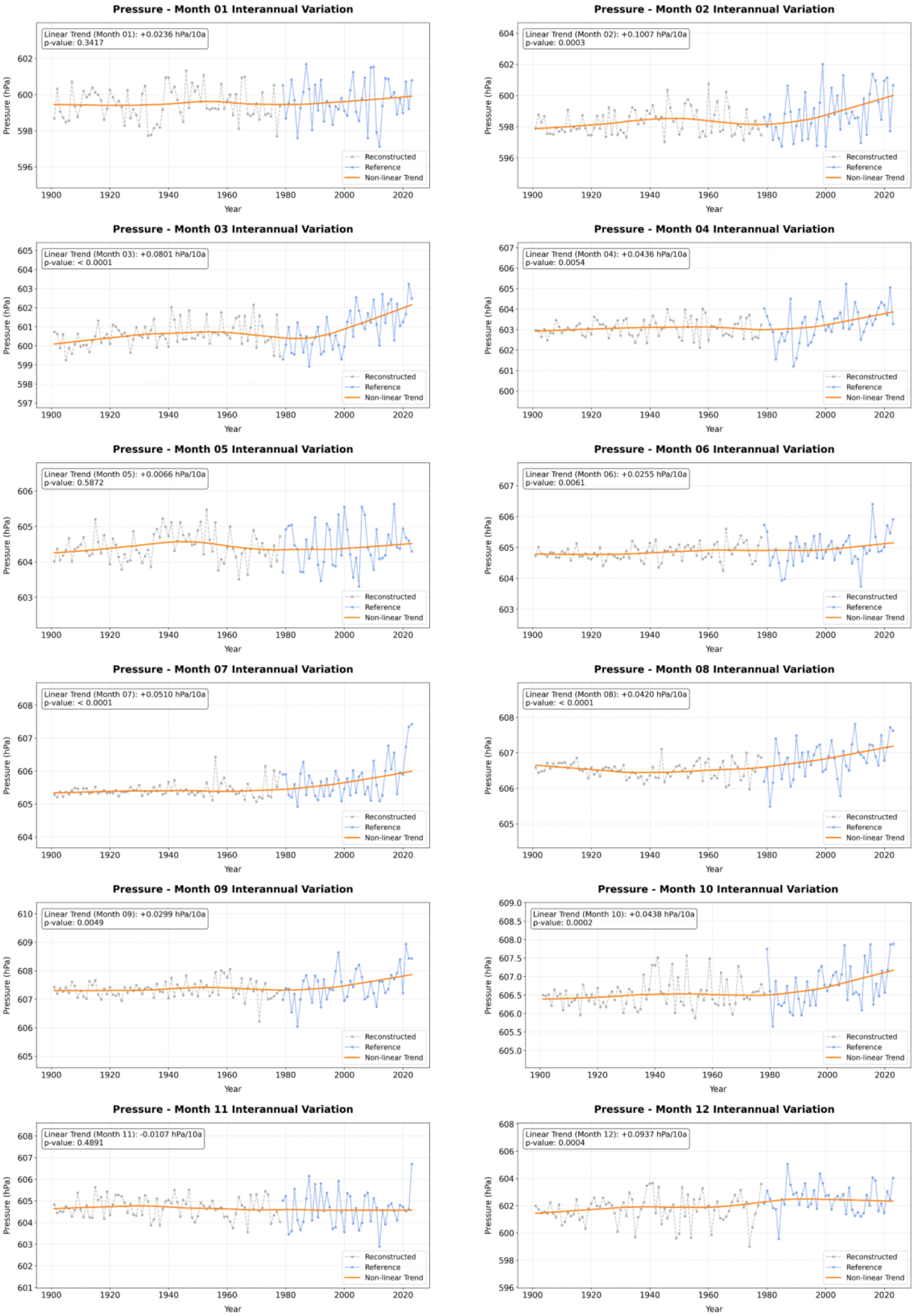

Figure S6. Monthly interannual variations of surface pressure over the Tibetan Plateau (1901–2023). Grey dashed and solid blue lines denote the reconstructed (1901–1978) and reference (1979–2023) data, respectively. The orange curve indicates the trend.

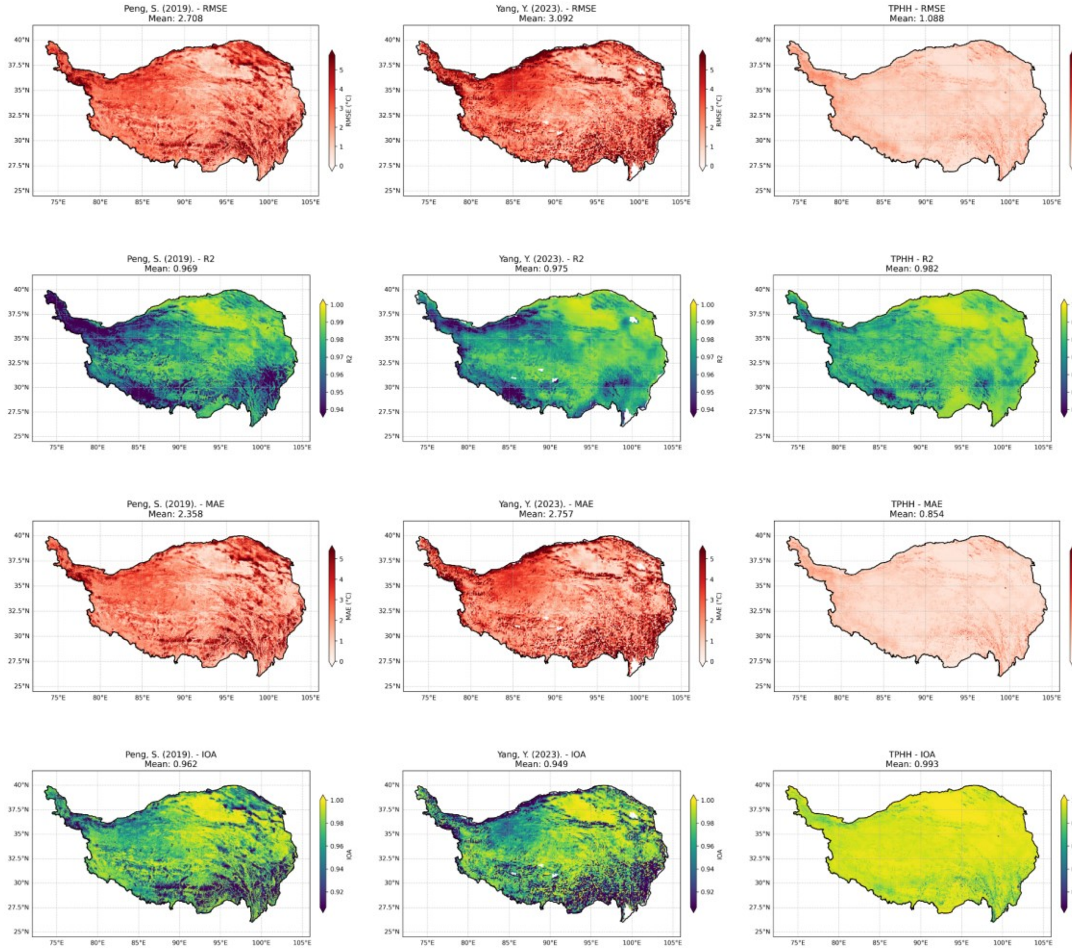

Figure S7. The panel compares the proposed TPHH product against two representative datasets: a delta-downscaling-based product (Peng, S., 2019) and a GAN-based deep-learning product (Yang, Y., 2023), using TPMFD as the benchmark. Metrics include the coefficient of determination (R^2), Root Mean Square Error (RMSE), Mean Absolute Error (MAE), and Index of Agreement (IOA).

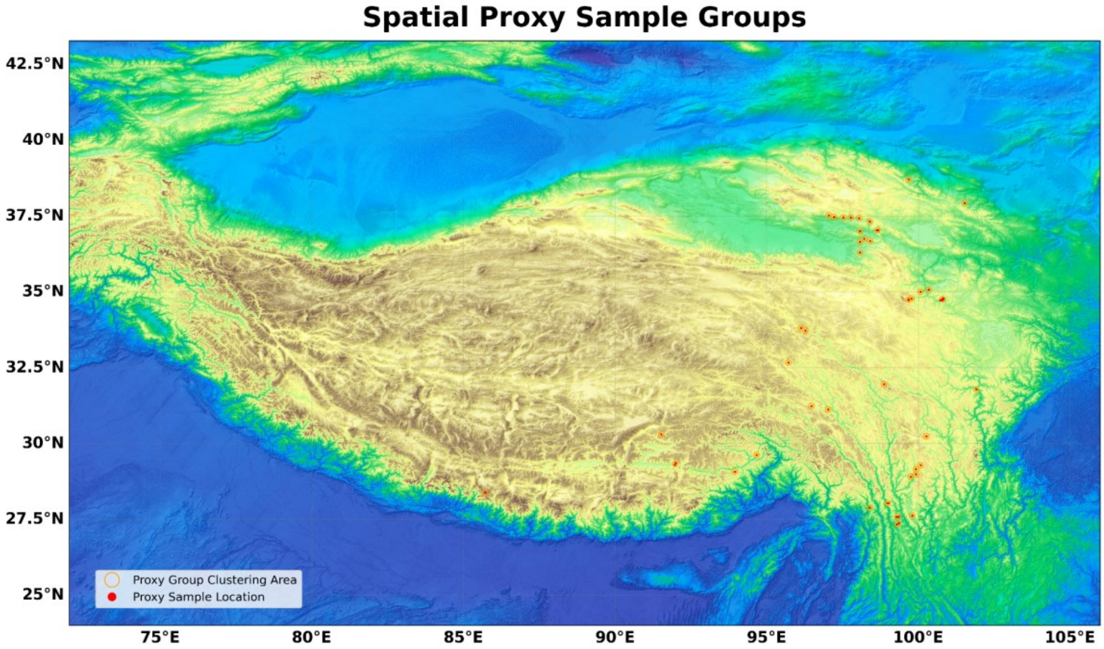

Figure S8. Geographical distribution of the 41 tree-ring proxy groups over the Tibetan Plateau used in this study. Symbols represent the precise locations of chronologies (red dots), while circles (orange) denote the spatial clustering areas defined for ternary regression fitting.

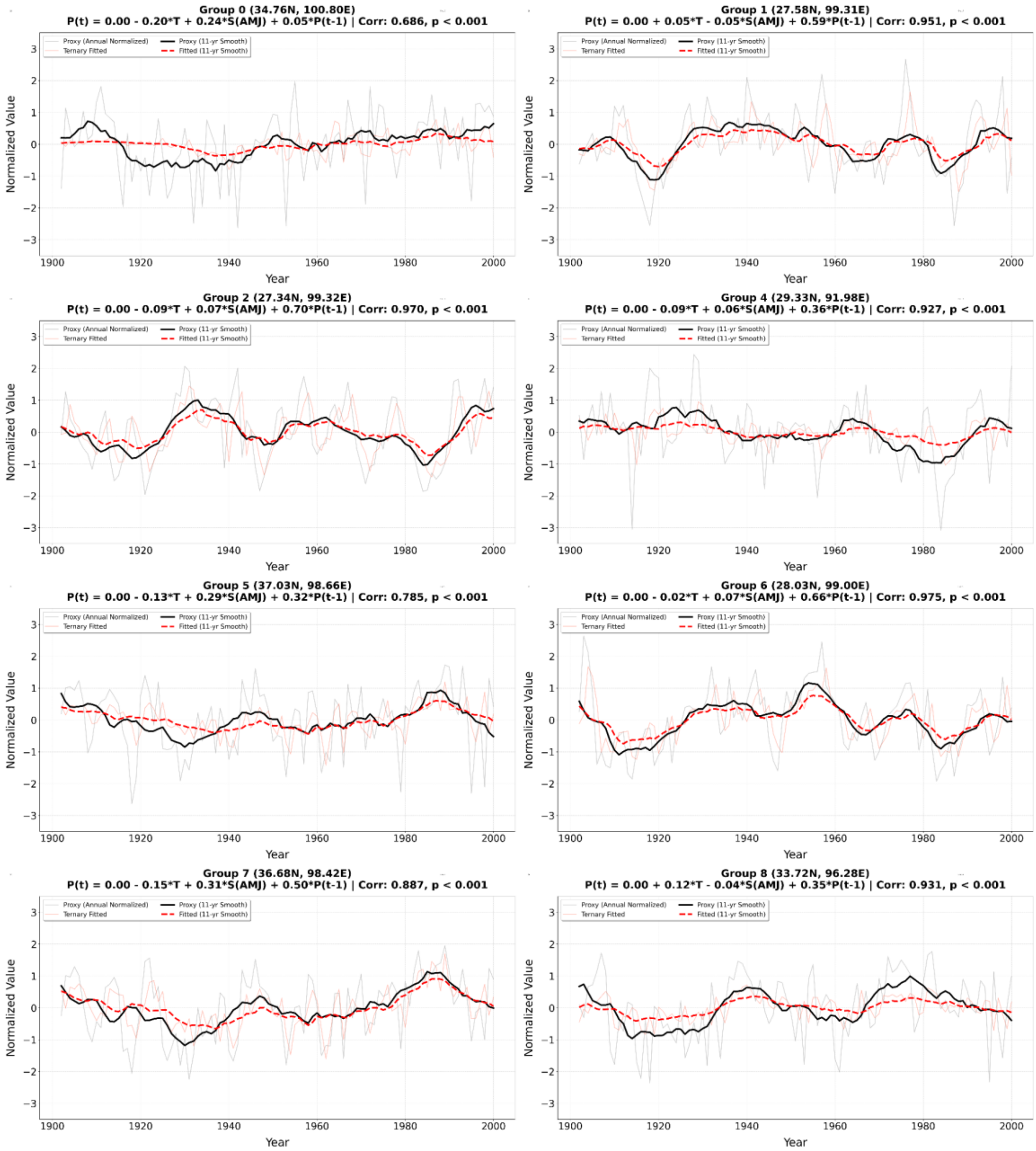

Figure S9. Temporal consistency between actual tree-ring proxy series and TPHH-based ternary fitted series for Groups 0–2 and 4–8 during 1901–2000. Each panel displays the annual normalized proxy values (light grey) and the 11-year moving average (black bold line), alongside the fitted series (light red line) and its 11-year smooth (red bold dashed line). The fitting equations, integrating JJA temperature (T), AMJ specific humidity (S), and lag -1 proxy memory (P(t-1)), are provided at the top of each subplot with their respective Pearson correlation coefficients (Corr.). (Note: Group 3 is presented in Figure 12 of the main text).

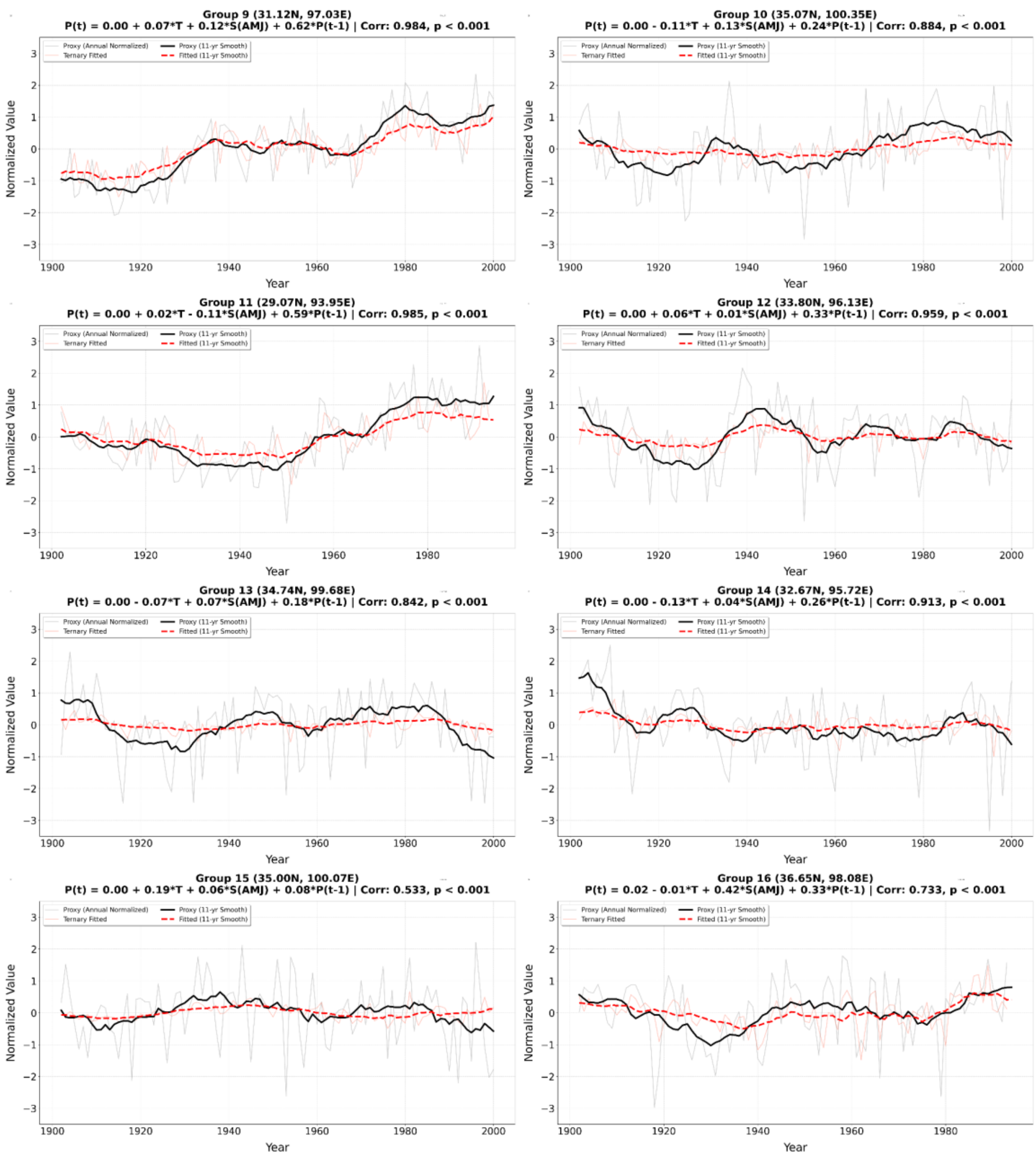

Figure S10. Temporal consistency between actual tree-ring proxy series and TPHH-based ternary fitted series for Groups 9-16 during 1901–2000. Each panel displays the annual normalized proxy values (light grey) and the 11-year moving average (black bold line), alongside the fitted series (light red line) and its 11-year smooth (red bold dashed line). The fitting equations, integrating JJA temperature (T), AMJ specific humidity (S), and lag -1 proxy memory (P(t-1)), are provided at the top of each subplot with their respective Pearson correlation coefficients (Corr.).

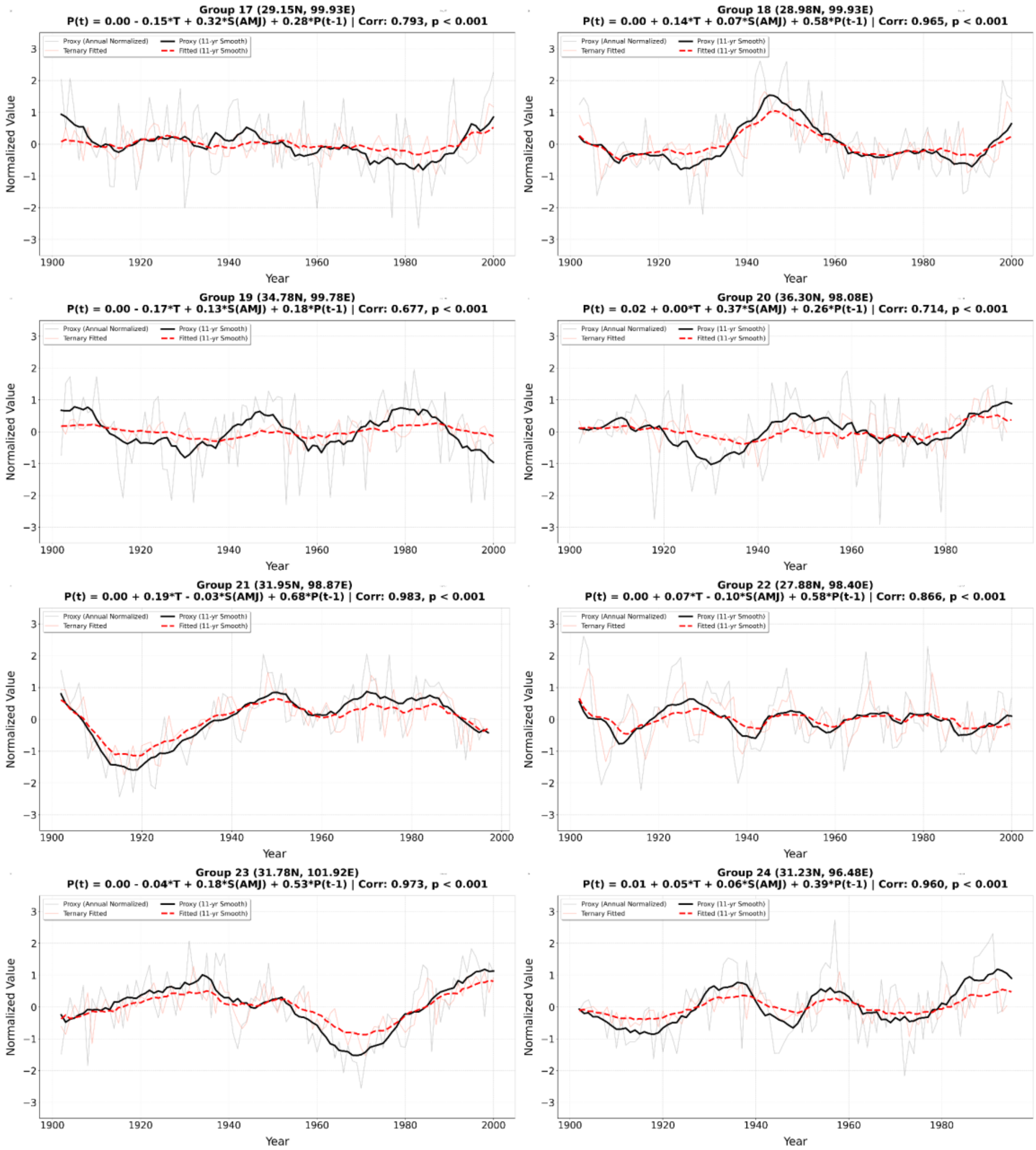

Figure S11. Temporal consistency between actual tree-ring proxy series and TPHH-based ternary fitted series for Groups 17-24 during 1901–2000. Each panel displays the annual normalized proxy values (light grey) and the 11-year moving average (black bold line), alongside the fitted series (light red line) and its 11-year smooth (red bold dashed line). The fitting equations, integrating JJA temperature (T), AMJ specific humidity (S), and lag -1 proxy memory (P(t-1)), are provided at the top of each subplot with their respective Pearson correlation coefficients (Corr.).

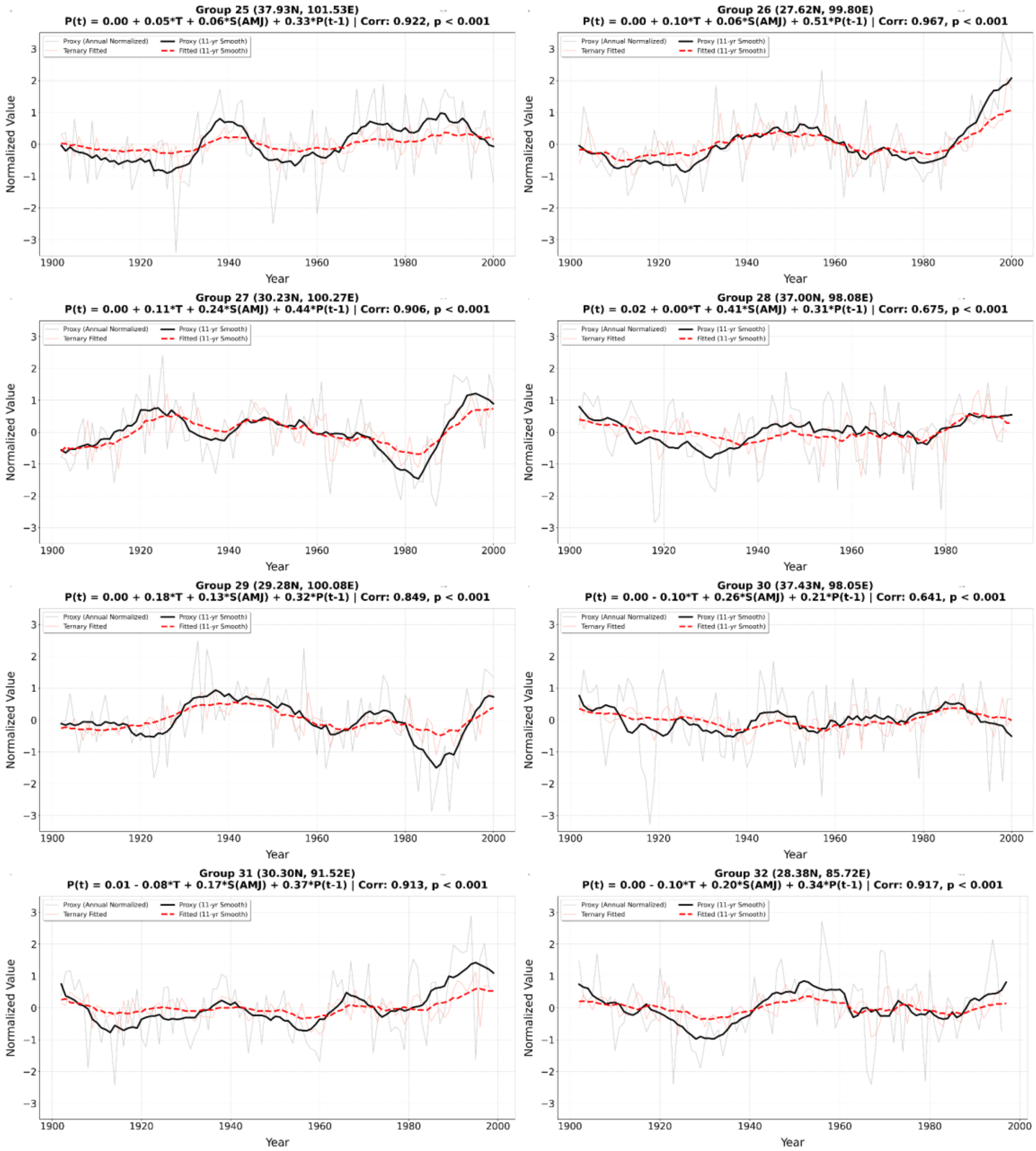

Figure S12. Temporal consistency between actual tree-ring proxy series and TPHH-based ternary fitted series for Groups 25-32 during 1901–2000. Each panel displays the annual normalized proxy values (light grey) and the 11-year moving average (black bold line), alongside the fitted series (light red line) and its 11-year smooth (red bold dashed line). The fitting equations, integrating JJA temperature (T), AMJ specific humidity (S), and lag -1 proxy memory (P(t-1)), are provided at the top of each subplot with their respective Pearson correlation coefficients (Corr.).

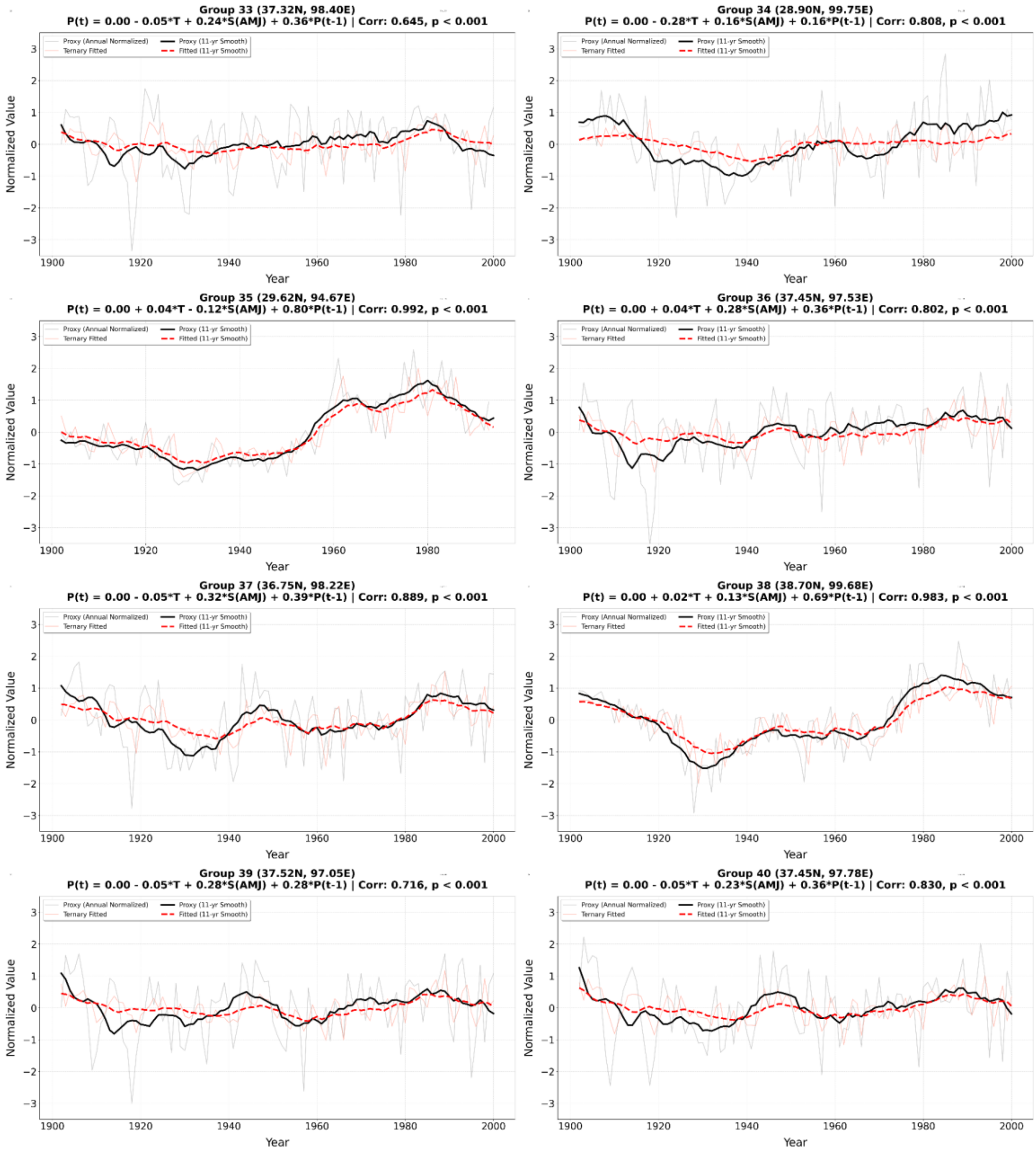

Figure S13. Temporal consistency between actual tree-ring proxy series and TPHH-based ternary fitted series for Groups 33-40 during 1901–2000. Each panel displays the annual normalized proxy values (light grey) and the 11-year moving average (black bold line), alongside the fitted series (light red line) and its 11-year smooth (red bold dashed line). The fitting equations, integrating JJA temperature (T), AMJ specific humidity (S), and lag -1 proxy memory (P(t-1)), are provided at the top of each subplot with their respective Pearson correlation coefficients (Corr.).

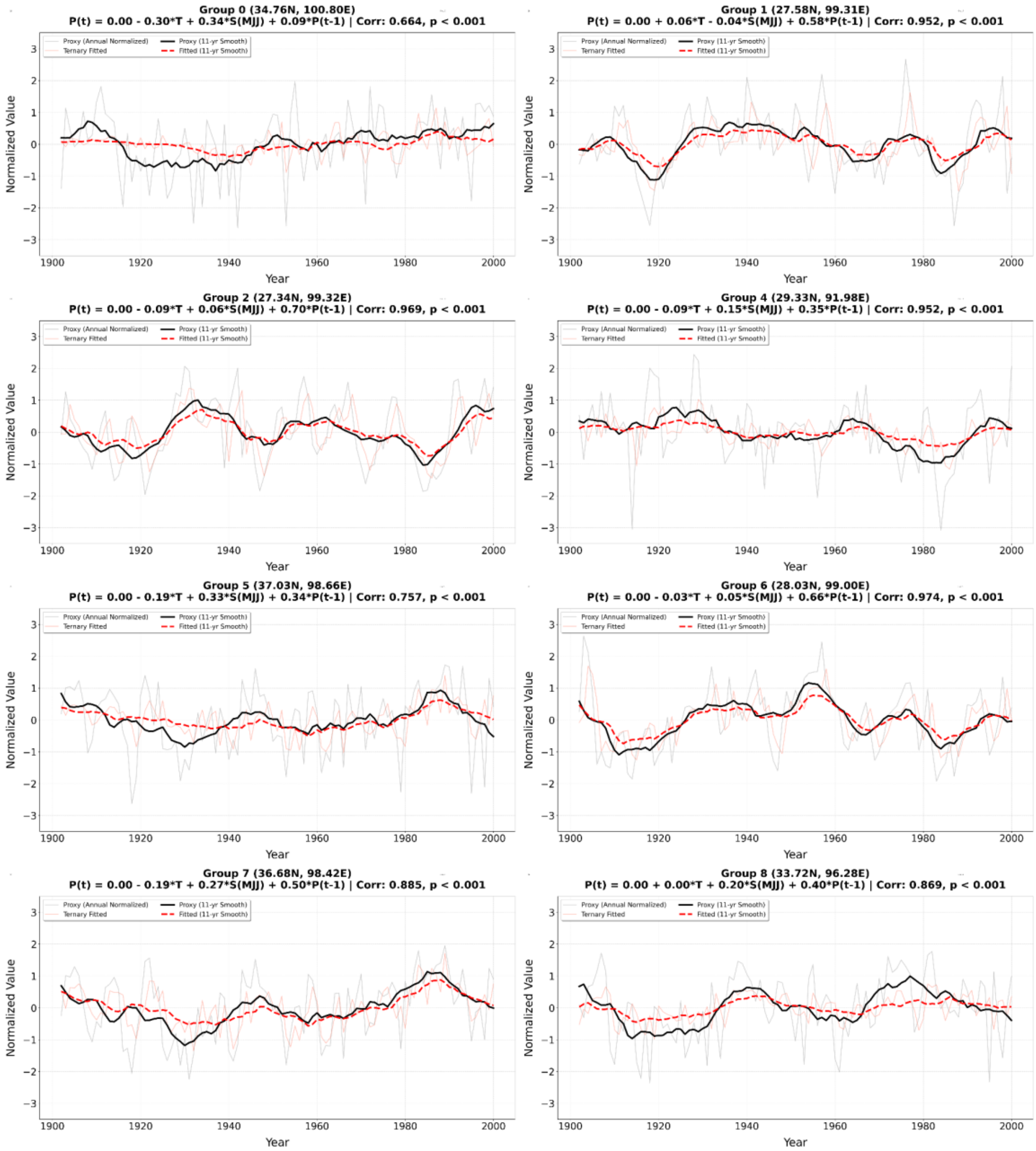

Figure S14. Temporal consistency between actual tree-ring proxy series and TPHH-based ternary fitted series for Groups 0–2 and 4–8 during 1901–2000. Each panel displays the annual normalized proxy values (light grey) and the 11-year moving average (black bold line), alongside the fitted series (light red line) and its 11-year smooth (red bold dashed line). The fitting equations, integrating JJA temperature (T), MJJ specific humidity (S), and lag -1 proxy memory (P(t-1)), are provided at the top of each subplot with their respective Pearson correlation coefficients (Corr.). (Note: Group 3 is presented in Figure 12 of the main text).

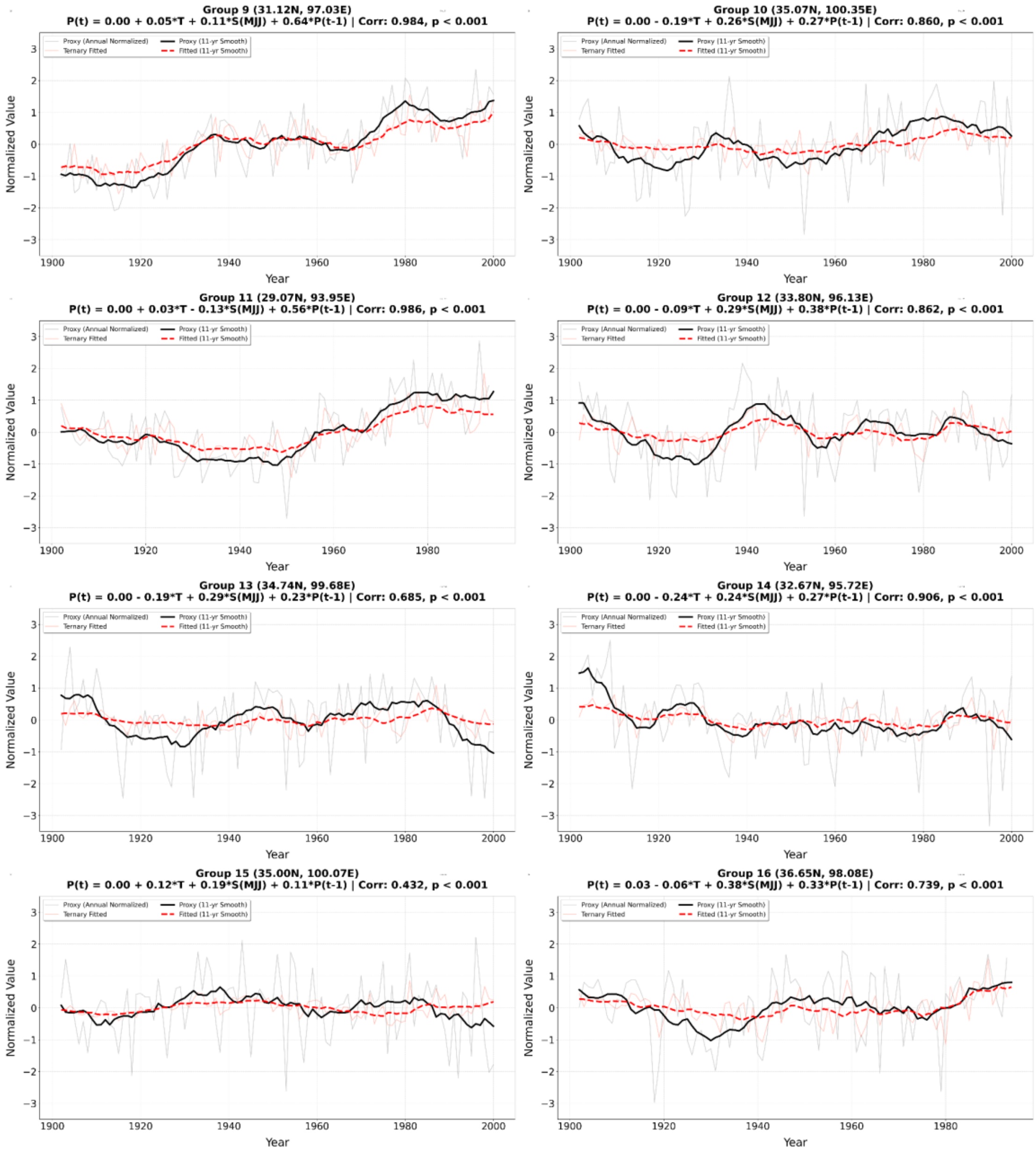

Figure S15. Temporal consistency between actual tree-ring proxy series and TPHH-based ternary fitted series for Groups 9-16 during 1901–2000. Each panel displays the annual normalized proxy values (light grey) and the 11-year moving average (black bold line), alongside the fitted series (light red line) and its 11-year smooth (red bold dashed line). The fitting equations, integrating JJA temperature (T), MJJ specific humidity (S), and lag -1 proxy memory (P(t-1)), are provided at the top of each subplot with their respective Pearson correlation coefficients (Corr.).

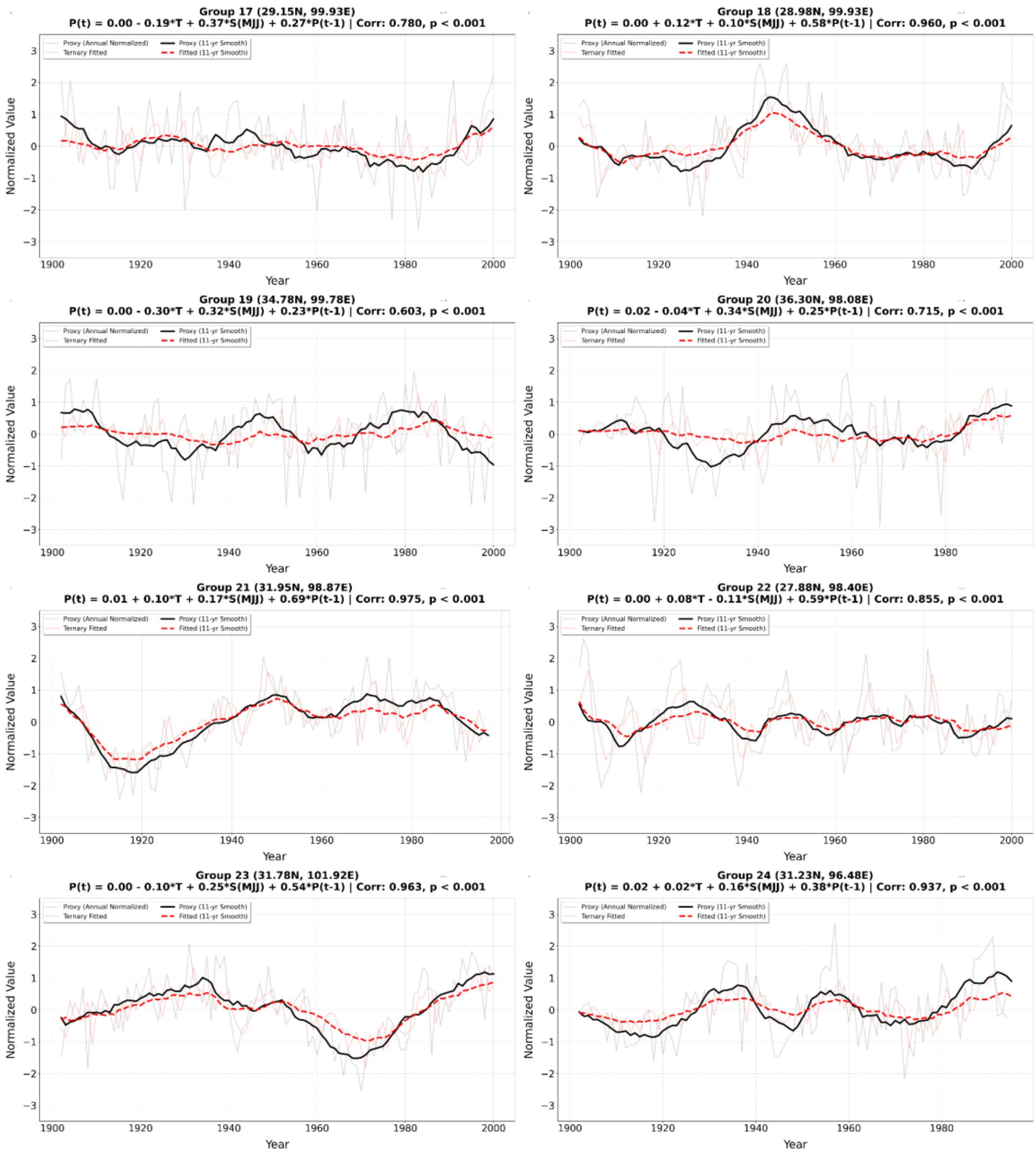

Figure S16. Temporal consistency between actual tree-ring proxy series and TPHH-based ternary fitted series for Groups 17-24 during 1901–2000. Each panel displays the annual normalized proxy values (light grey) and the 11-year moving average (black bold line), alongside the fitted series (light red line) and its 11-year smooth (red bold dashed line). The fitting equations, integrating JJA temperature (T), MJJ specific humidity (S), and lag -1 proxy memory (P(t-1)), are provided at the top of each subplot with their respective Pearson correlation coefficients (Corr.).

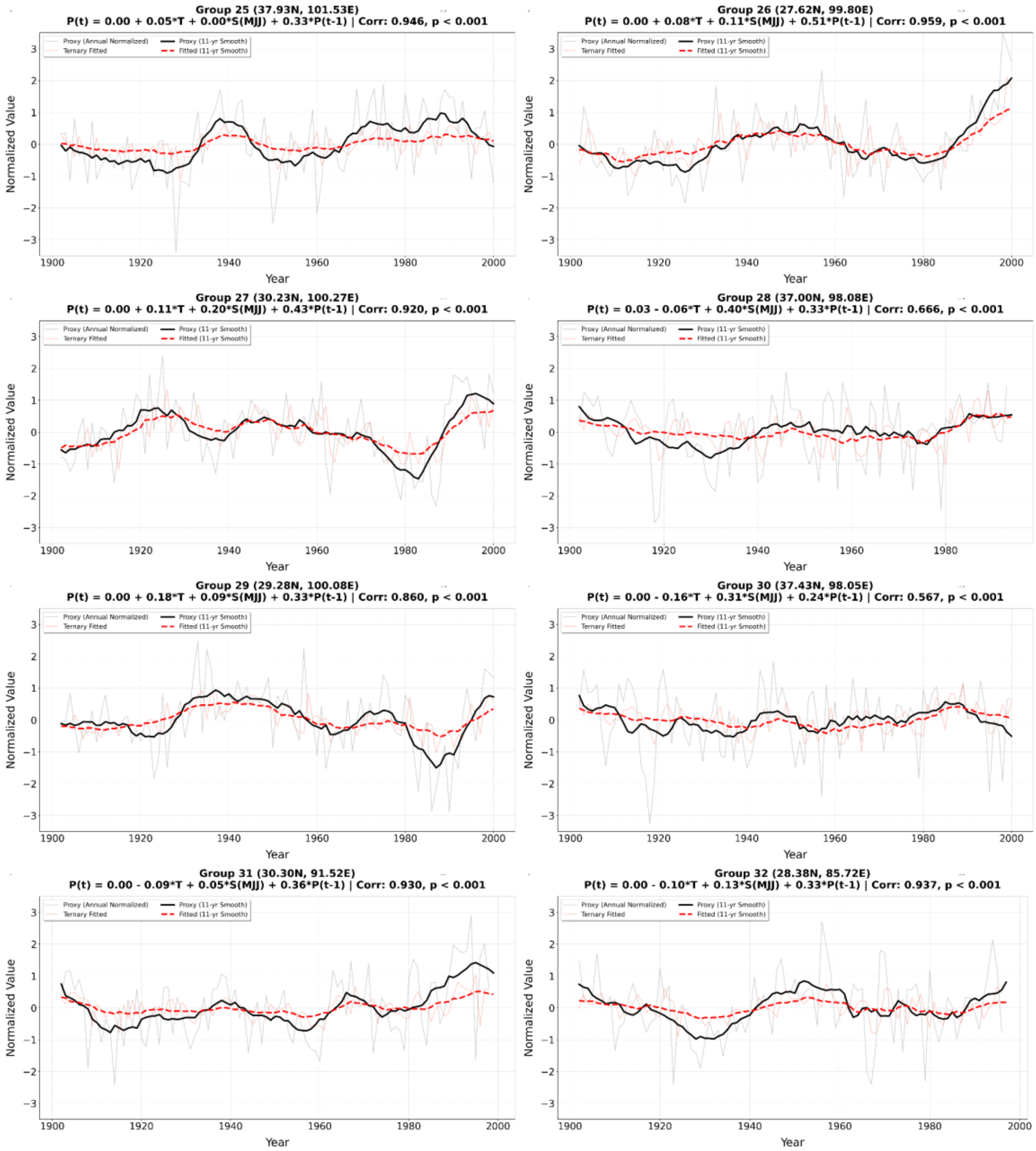

Figure S17. Temporal consistency between actual tree-ring proxy series and TPHH-based ternary fitted series for Groups 25-32 during 1901–2000. Each panel displays the annual normalized proxy values (light grey) and the 11-year moving average (black bold line), alongside the fitted series (light red line) and its 11-year smooth (red bold dashed line). The fitting equations, integrating JJA temperature (T), MJJ specific humidity (S), and lag -1 proxy memory (P(t-1)), are provided at the top of each subplot with their respective Pearson correlation coefficients (Corr.).

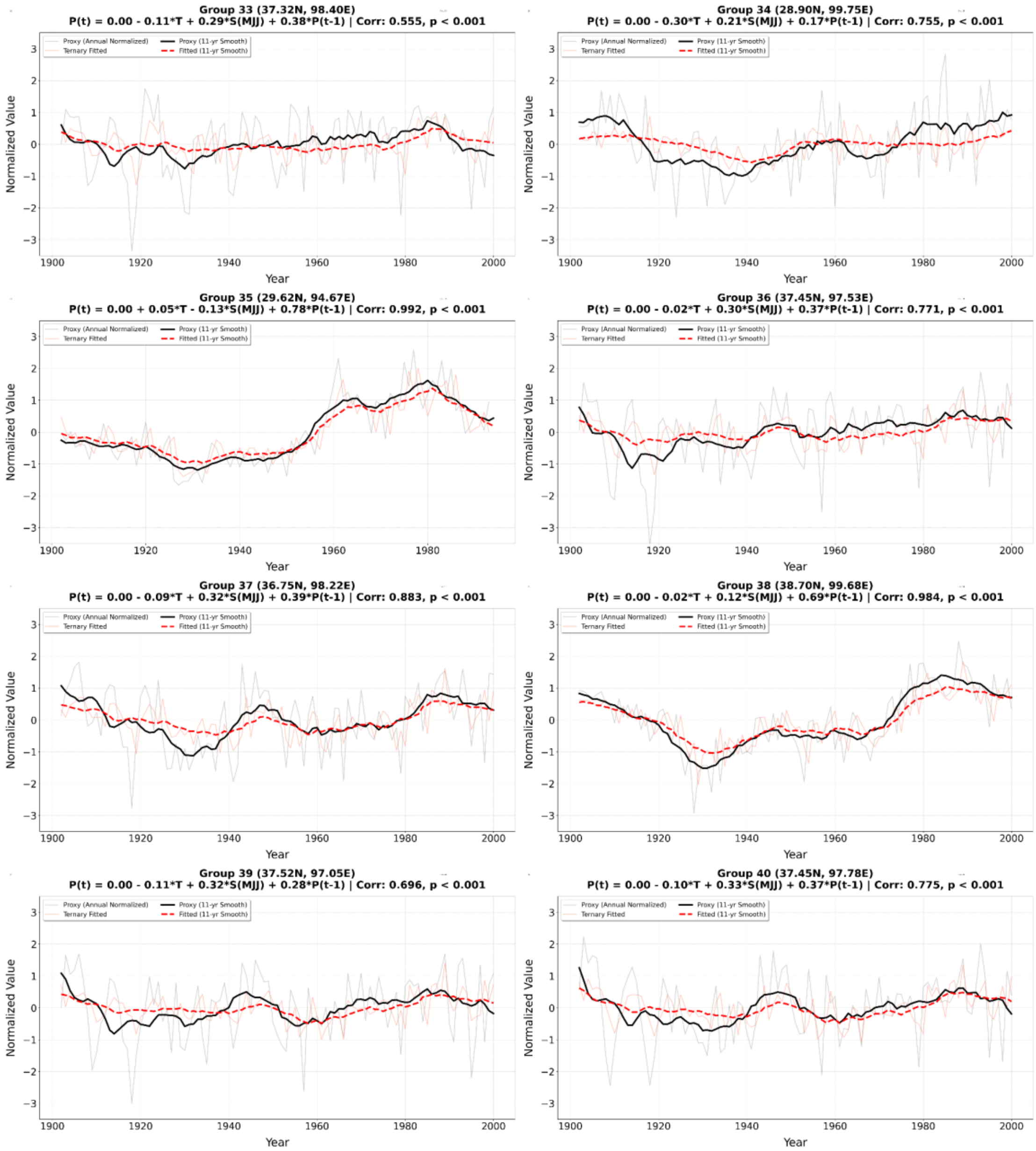

Figure S18. Temporal consistency between actual tree-ring proxy series and TPHH-based ternary fitted series for Groups 33-40 during 1901–2000. Each panel displays the annual normalized proxy values (light grey) and the 11-year moving average (black bold line), alongside the fitted series (light red line) and its 11-year smooth (red bold dashed line). The fitting equations, integrating JJA temperature (T), MJJ specific humidity (S), and lag -1 proxy memory (P(t-1)), are provided at the top of each subplot with their respective Pearson correlation coefficients (Corr.).

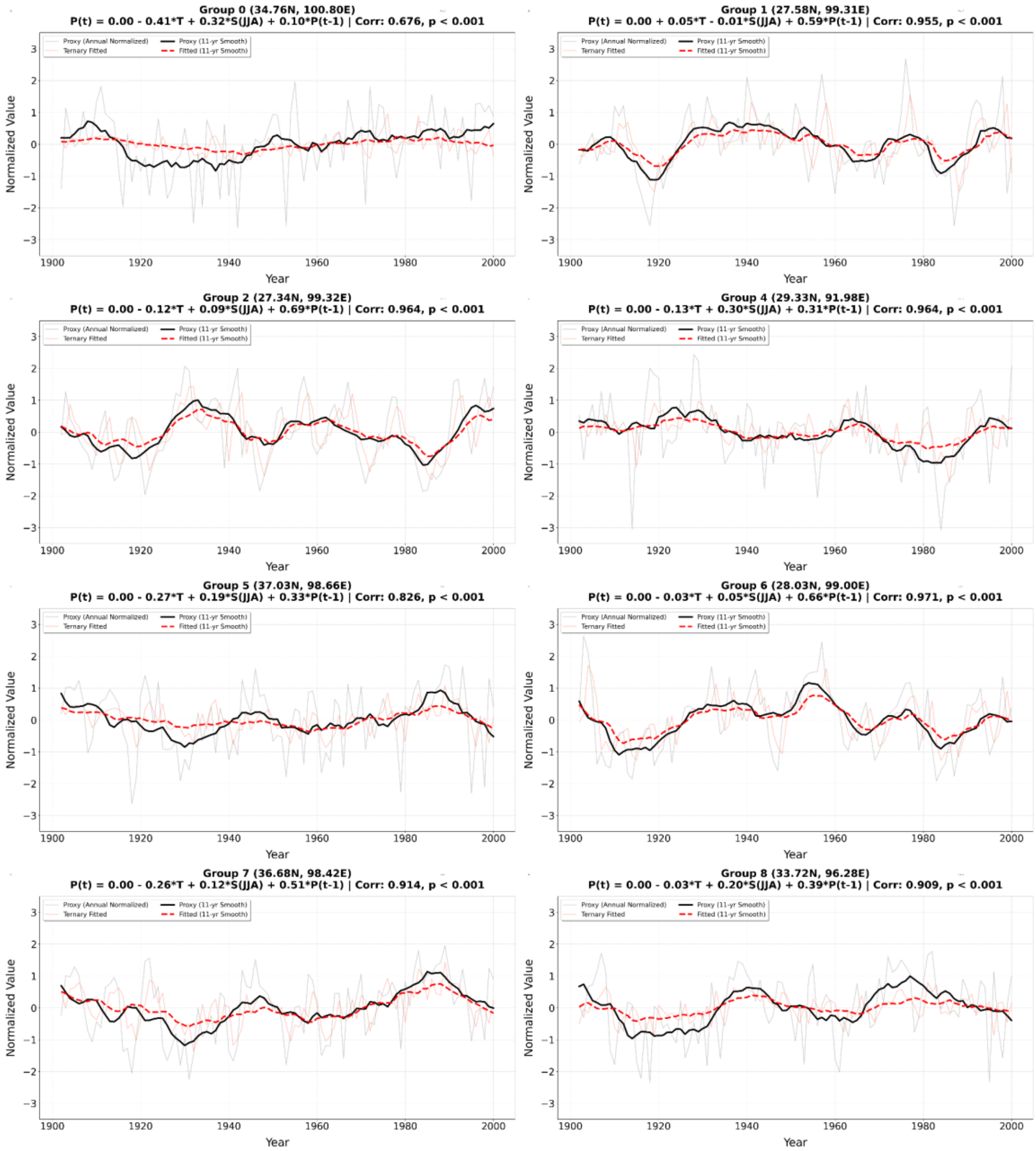

Figure S19. Temporal consistency between actual tree-ring proxy series and TPHH-based ternary fitted series for Groups 0–2 and 4–8 during 1901–2000. Each panel displays the annual normalized proxy values (light grey) and the 11-year moving average (black bold line), alongside the fitted series (light red line) and its 11-year smooth (red bold dashed line). The fitting equations, integrating JJA temperature (T), JJA specific humidity (S), and lag -1 proxy memory (P(t-1)), are provided at the top of each subplot with their respective Pearson correlation coefficients (Corr.). (Note: Group 3 is presented in Figure 12 of the main text).

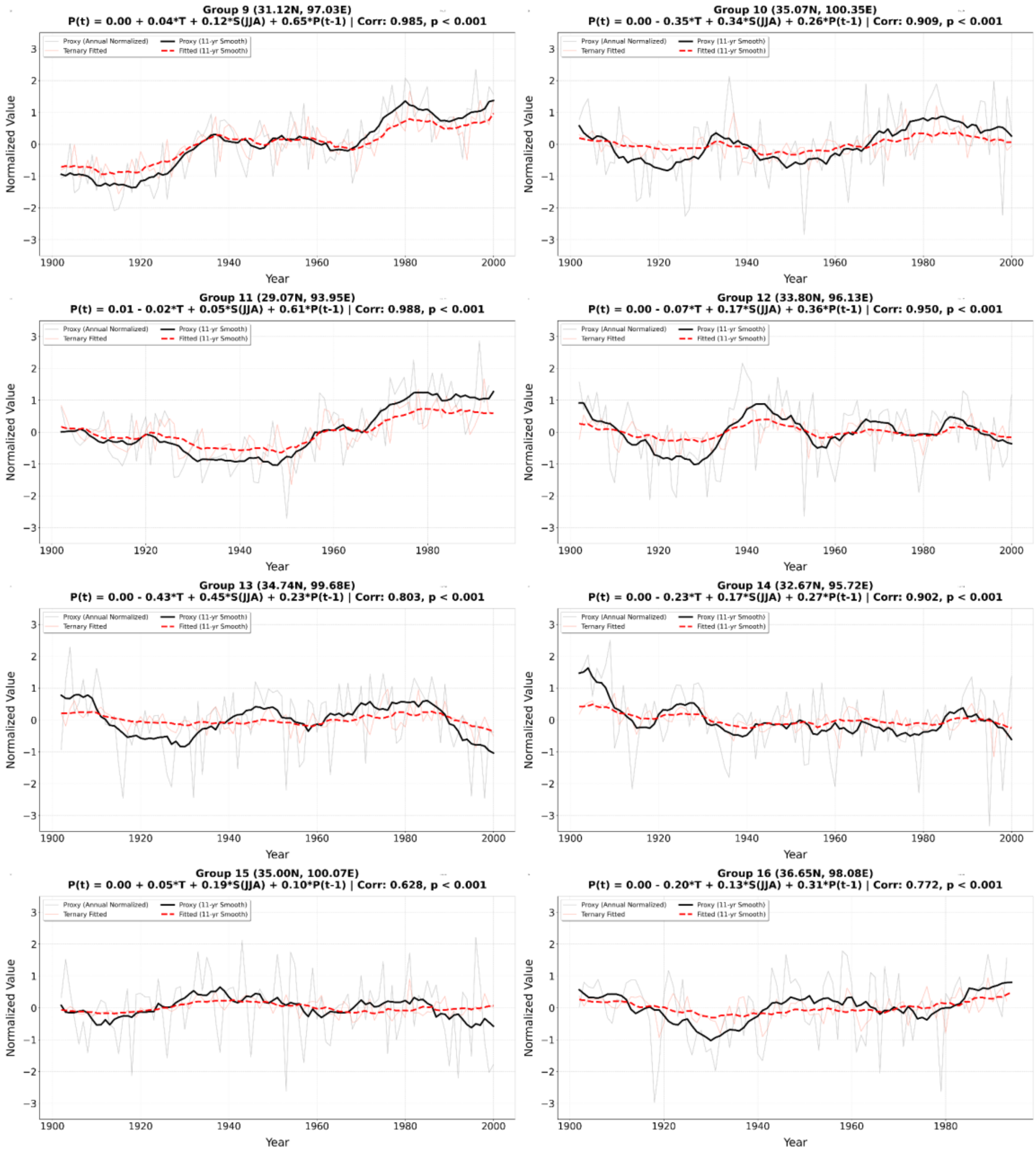

Figure S20. Temporal consistency between actual tree-ring proxy series and TPHH-based ternary fitted series for Groups 9-16 during 1901–2000. Each panel displays the annual normalized proxy values (light grey) and the 11-year moving average (black bold line), alongside the fitted series (light red line) and its 11-year smooth (red bold dashed line). The fitting equations, integrating JJA temperature (T), JJA specific humidity (S), and lag -1 proxy memory (P(t-1)), are provided at the top of each subplot with their respective Pearson correlation coefficients (Corr.).

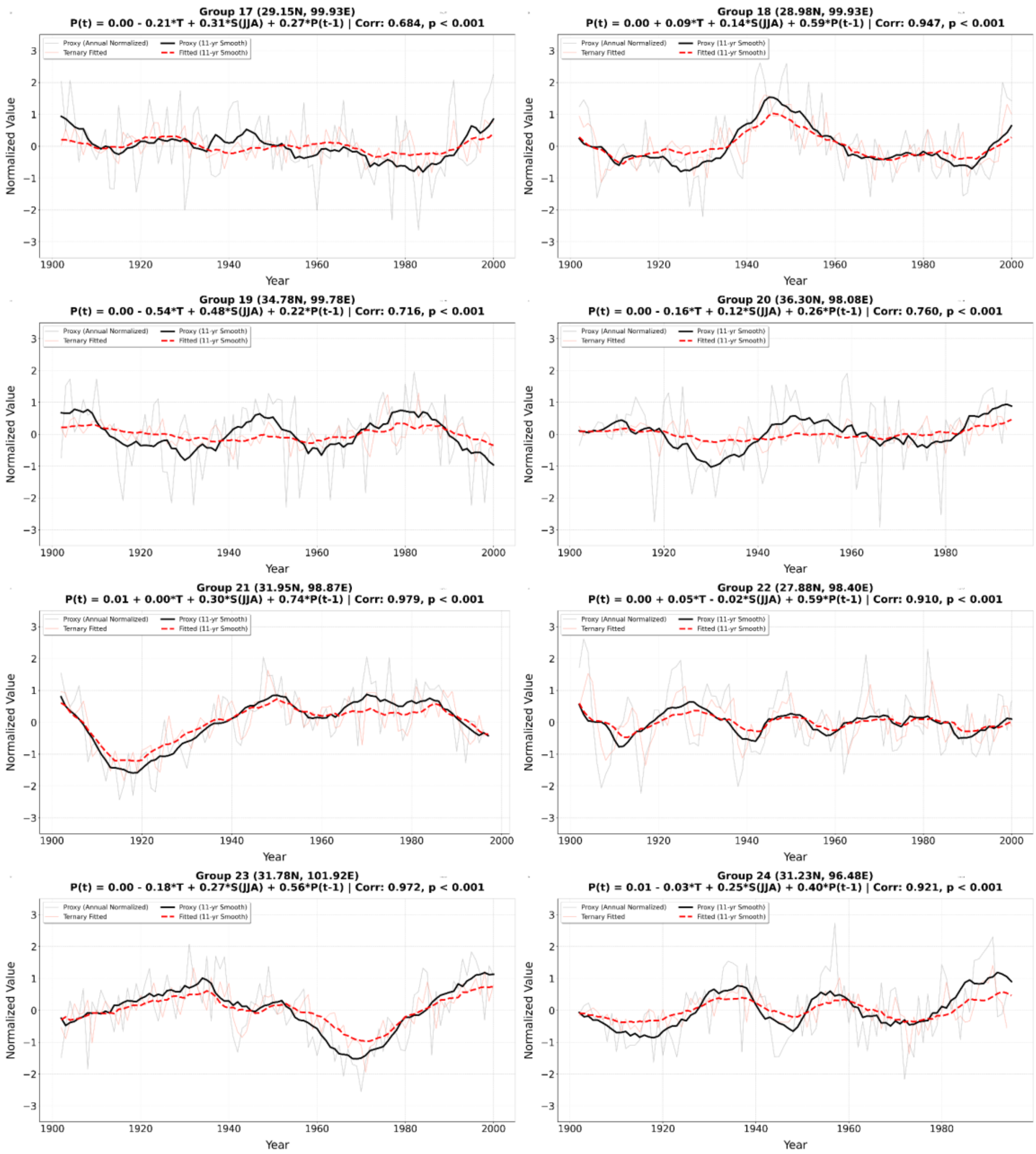

Figure S21. Temporal consistency between actual tree-ring proxy series and TPHH-based ternary fitted series for Groups 17-24 during 1901–2000. Each panel displays the annual normalized proxy values (light grey) and the 11-year moving average (black bold line), alongside the fitted series (light red line) and its 11-year smooth (red bold dashed line). The fitting equations, integrating JJA temperature (T), JJA specific humidity (S), and lag -1 proxy memory (P(t-1)), are provided at the top of each subplot with their respective Pearson correlation coefficients (Corr.).

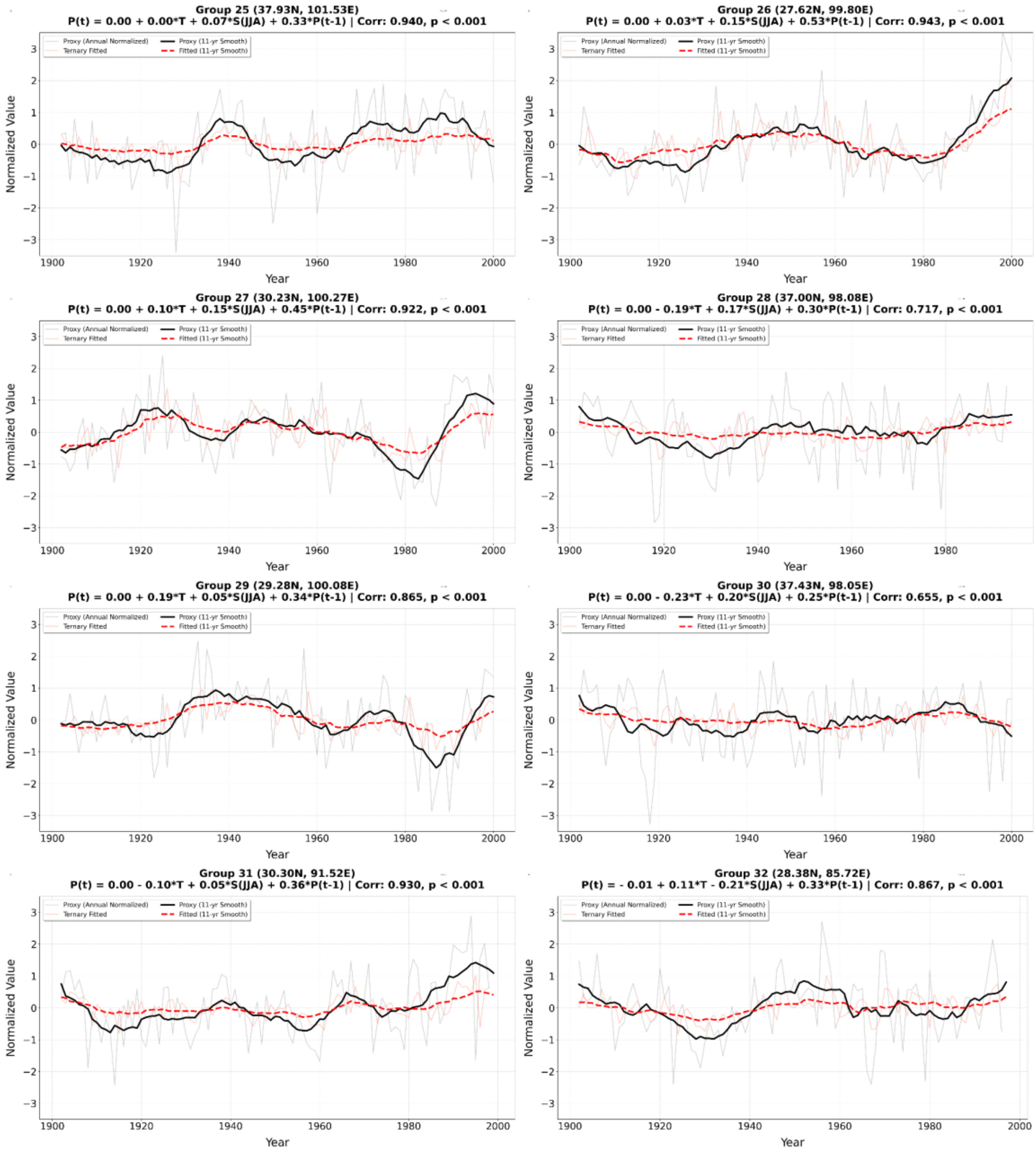

Figure S22. Temporal consistency between actual tree-ring proxy series and TPHH-based ternary fitted series for Groups 25-32 during 1901–2000. Each panel displays the annual normalized proxy values (light grey) and the 11-year moving average (black bold line), alongside the fitted series (light red line) and its 11-year smooth (red bold dashed line). The fitting equations, integrating JJA temperature (T), JJA specific humidity (S), and lag -1 proxy memory (P(t-1)), are provided at the top of each subplot with their respective Pearson correlation coefficients (Corr.).

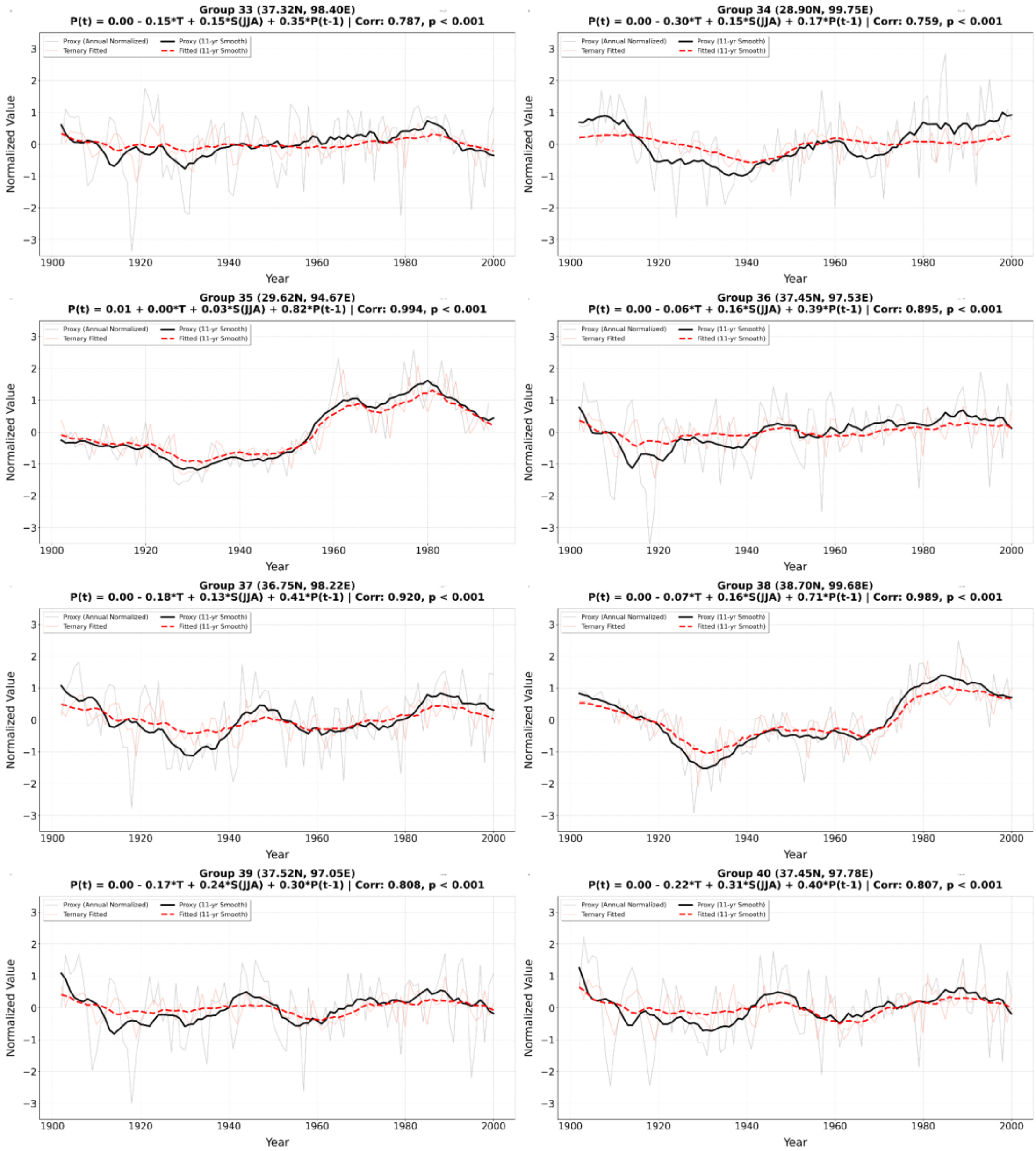

Figure S23. Temporal consistency between actual tree-ring proxy series and TPHH-based ternary fitted series for Groups 33-40 during 1901–2000. Each panel displays the annual normalized proxy values (light grey) and the 11-year moving average (black bold line), alongside the fitted series (light red line) and its 11-year smooth (red bold dashed line). The fitting equations, integrating JJA temperature (T), JJA specific humidity (S), and lag -1 proxy memory (P(t-1)), are provided at the top of each subplot with their respective Pearson correlation coefficients (Corr.).

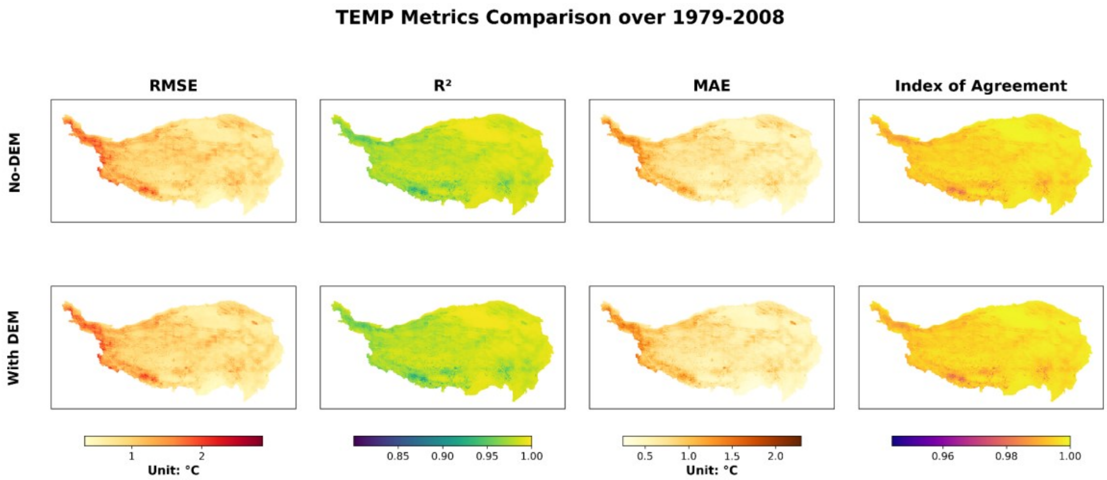

Figure S24. Metric map for temperature during 1979−2008 with DEM ablation experiment.

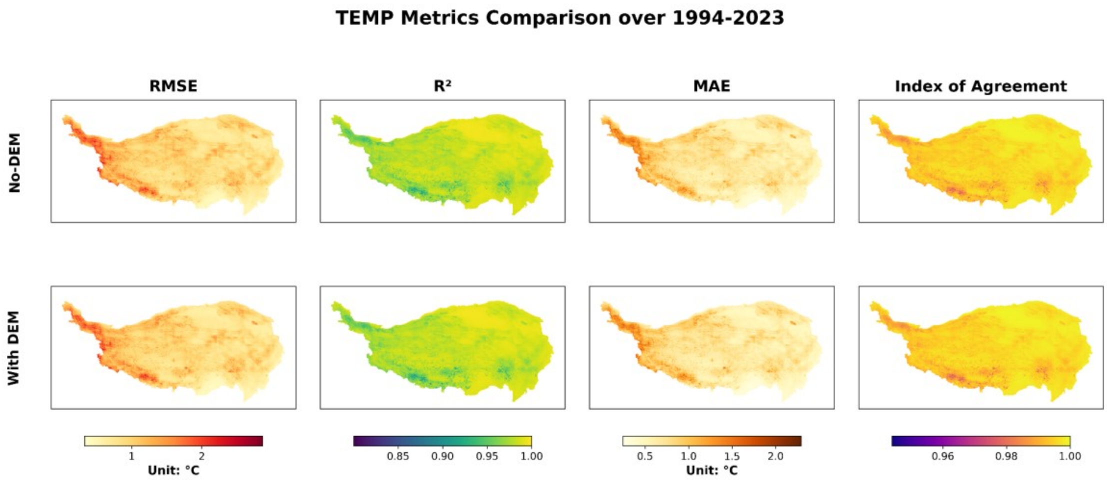

Figure S25. Metric map for temperature during 1994−2023 with DEM ablation experiment.

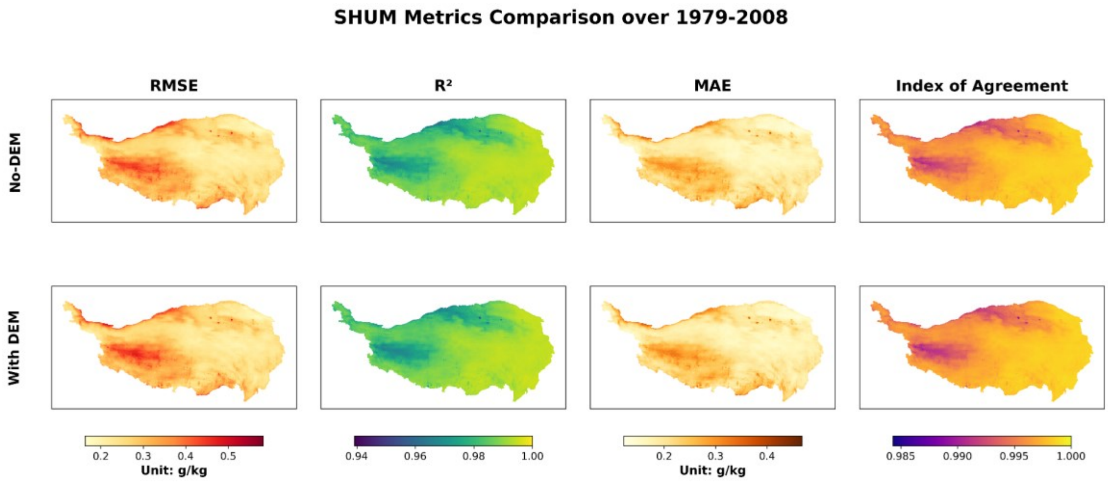

Figure S26. Metric map for specific humidity during 1979−2008 with DEM ablation experiment.

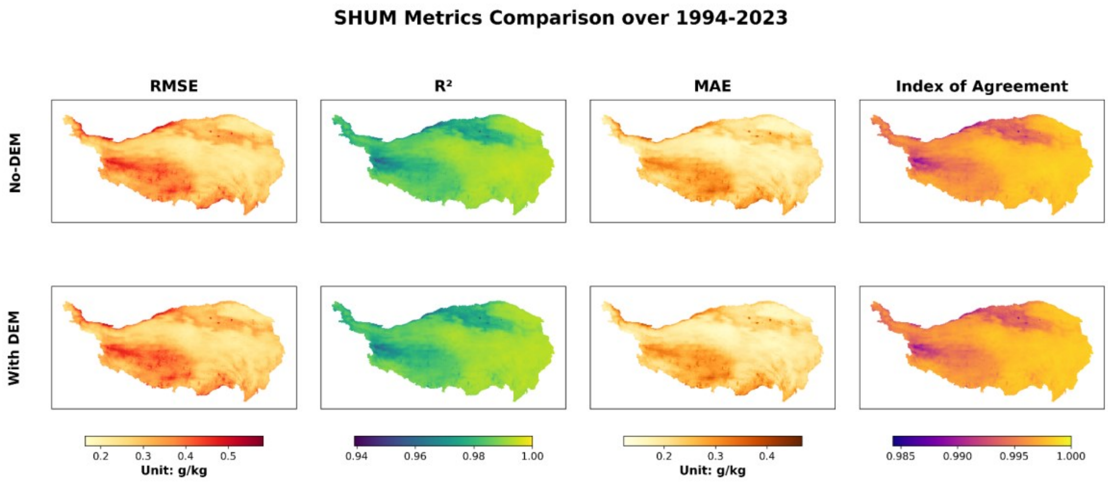

Figure S27. Metric map for specific humidity during 1994−2023 with DEM ablation experiment.

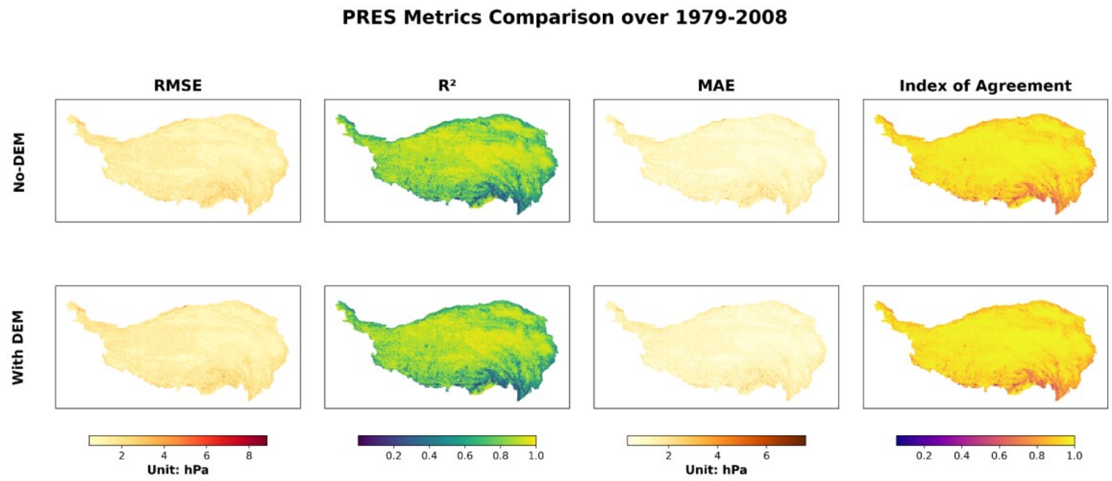

Figure S28. Metric map for pressure during 1979−2008 with DEM ablation experiment.

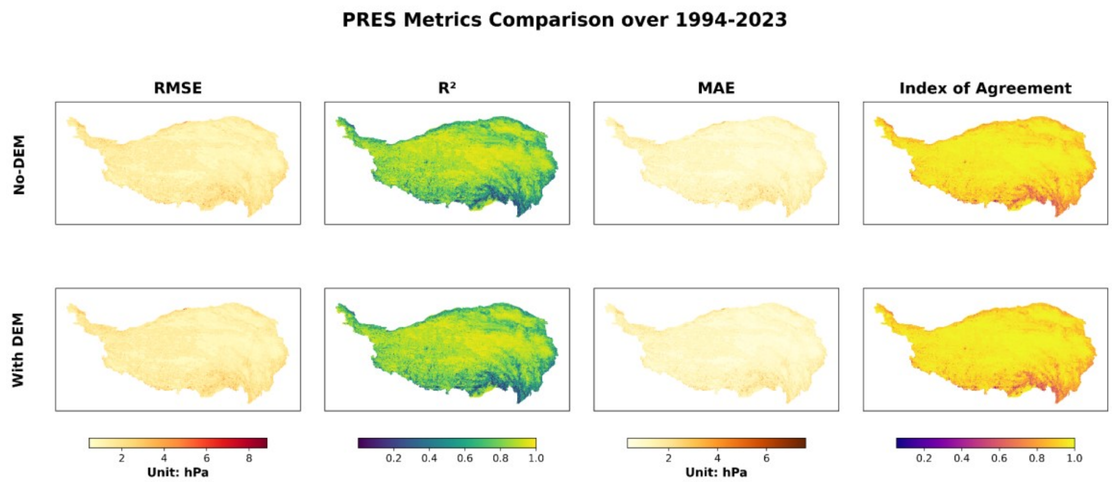

Figure S29. Metric map for pressure during 1994−2023 with DEM ablation experiment.

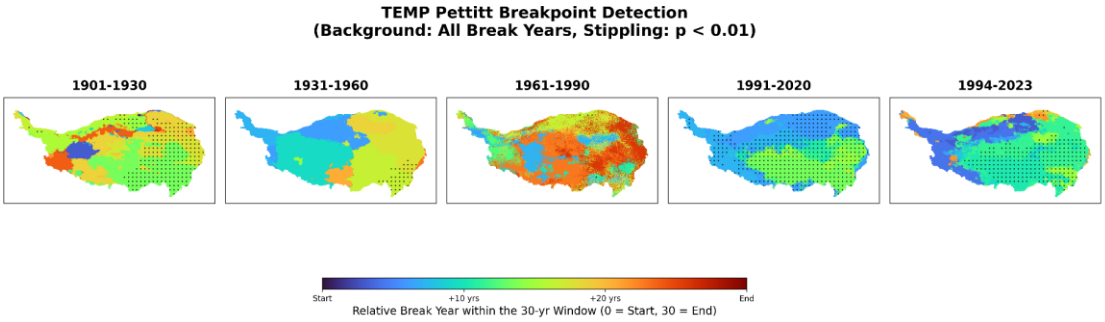

Figure S30. Pettitt breakpoint detection pattern of temperature over the Tibetan Plateau.

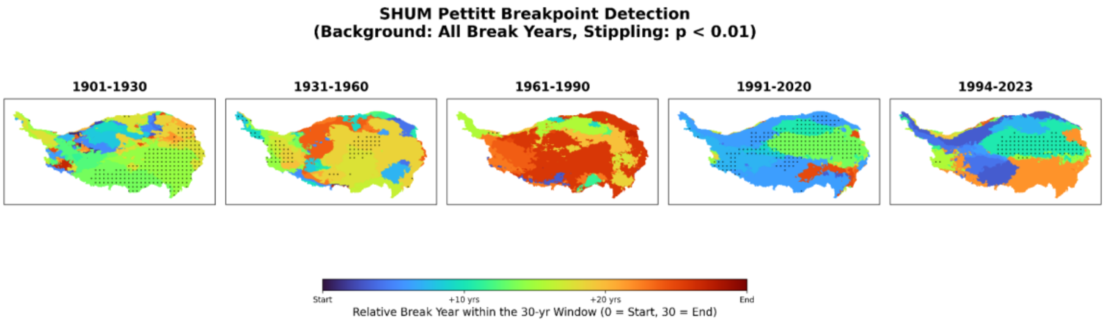

Figure S31. Pettitt breakpoint detection pattern of specific humidity over the Tibetan Plateau.

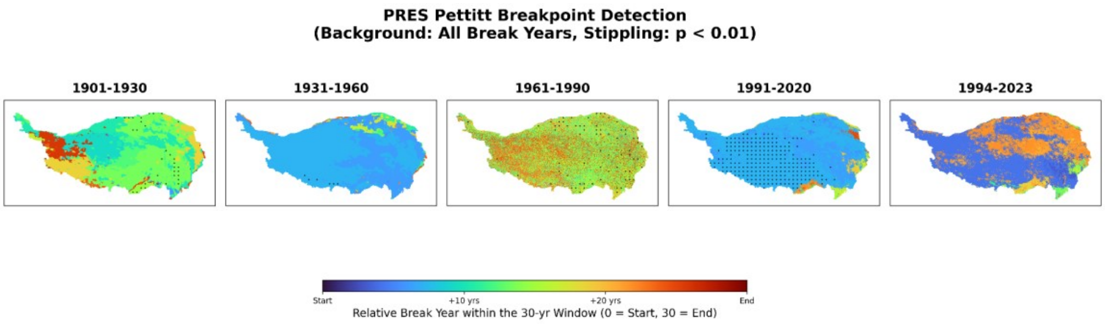

Figure S32. Pettitt breakpoint detection pattern of pressure over the Tibetan Plateau.

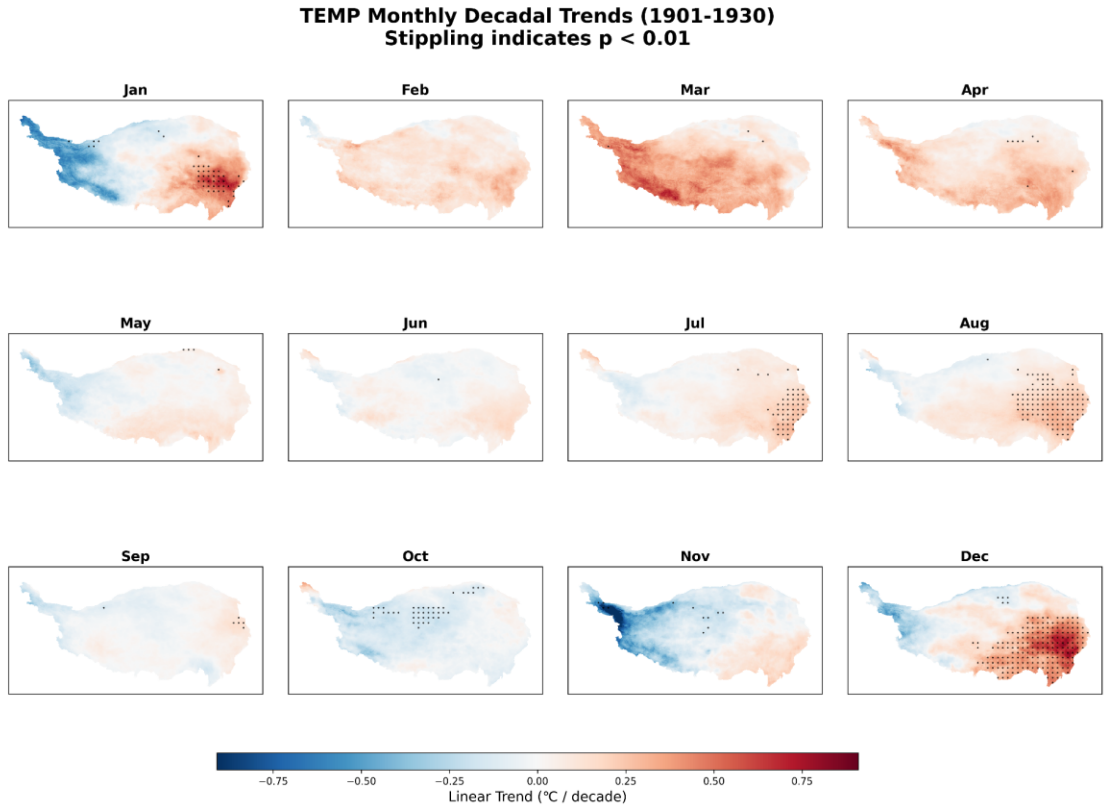

Figure S33. Temperature trends for each calendar month over the Tibetan Plateau during 1901-1930.

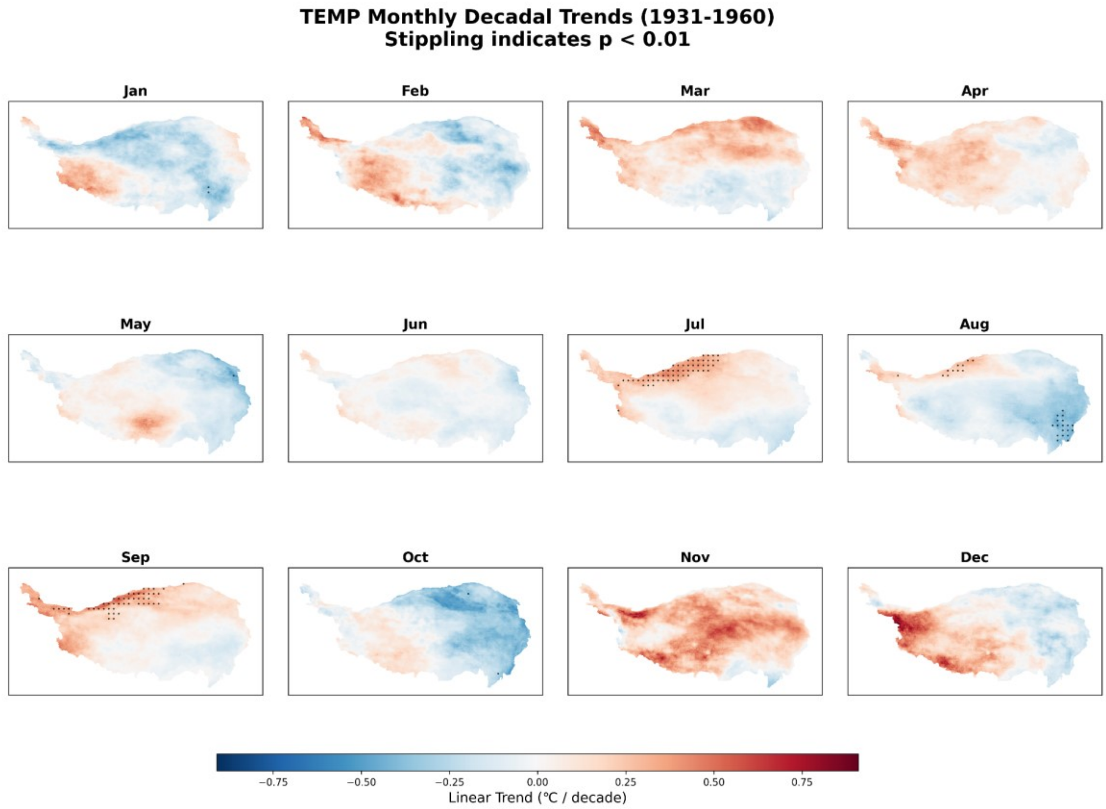

Figure S34. Temperature trends for each calendar month over the Tibetan Plateau during 1931-1960.

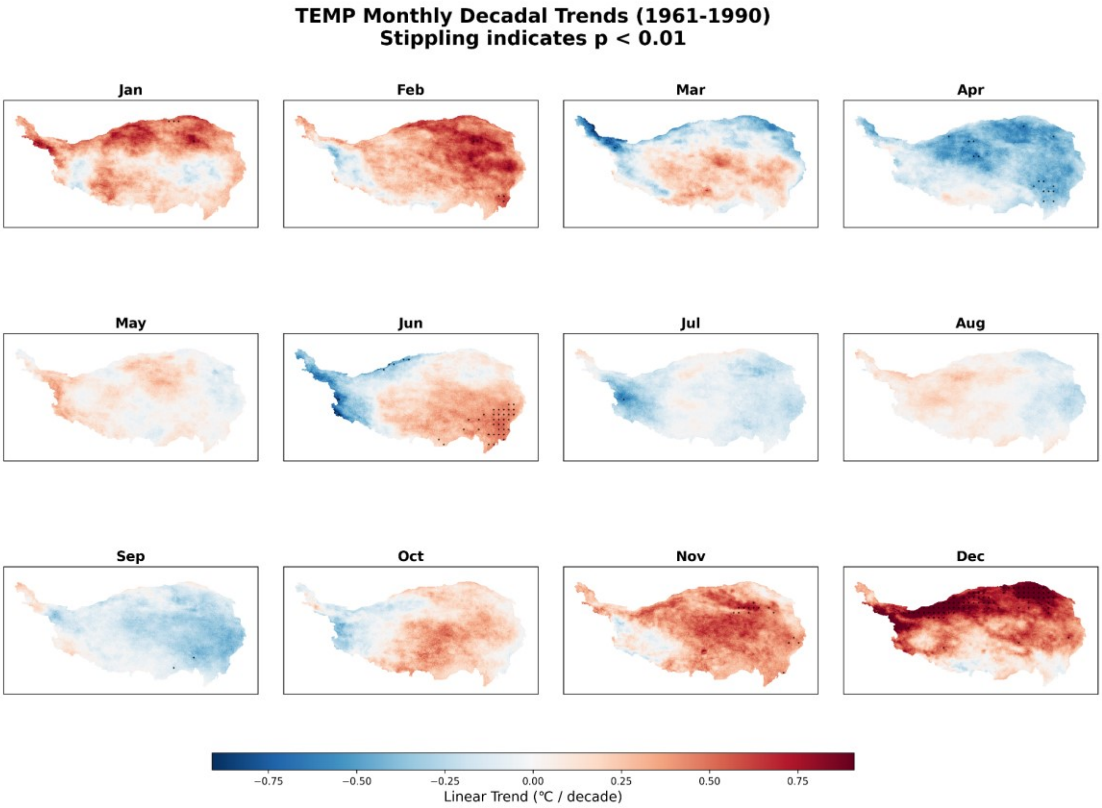

Figure S35. Temperature trends for each calendar month over the Tibetan Plateau during 1961-1990.

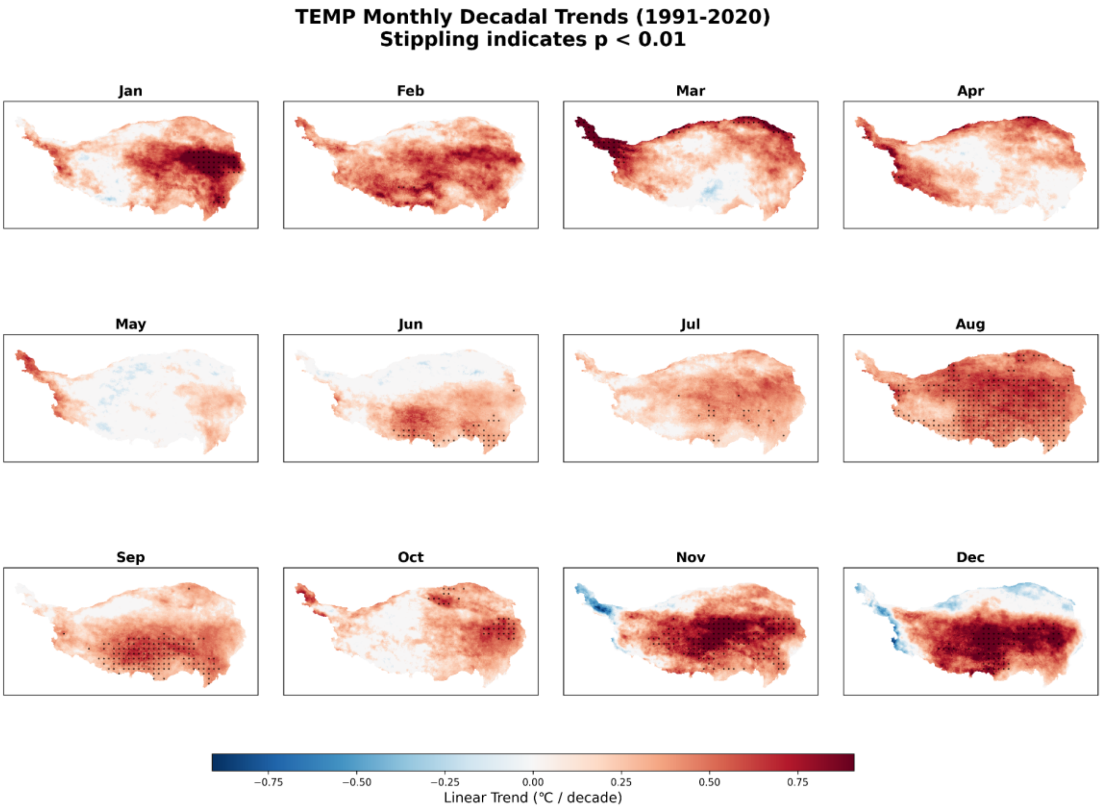

Figure S36. Temperature trends for each calendar month over the Tibetan Plateau during 1991-2020.

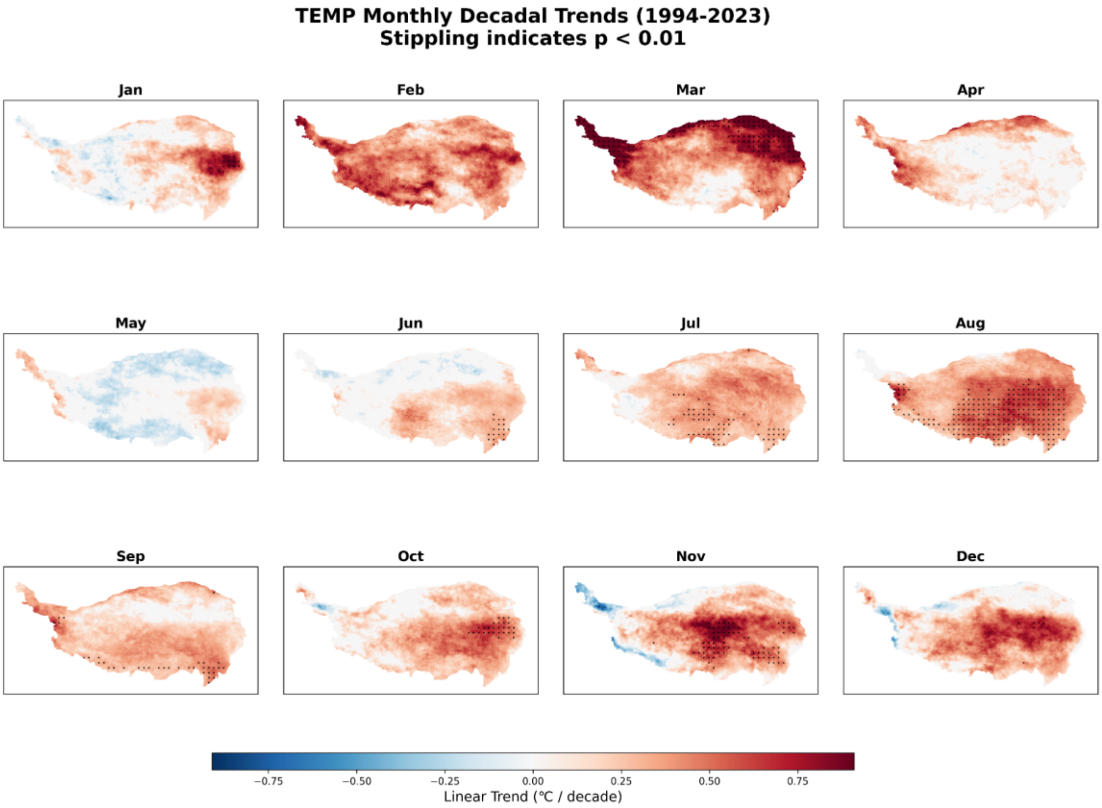

Figure S37. Temperature trends for each calendar month over the Tibetan Plateau during 1994-2023.

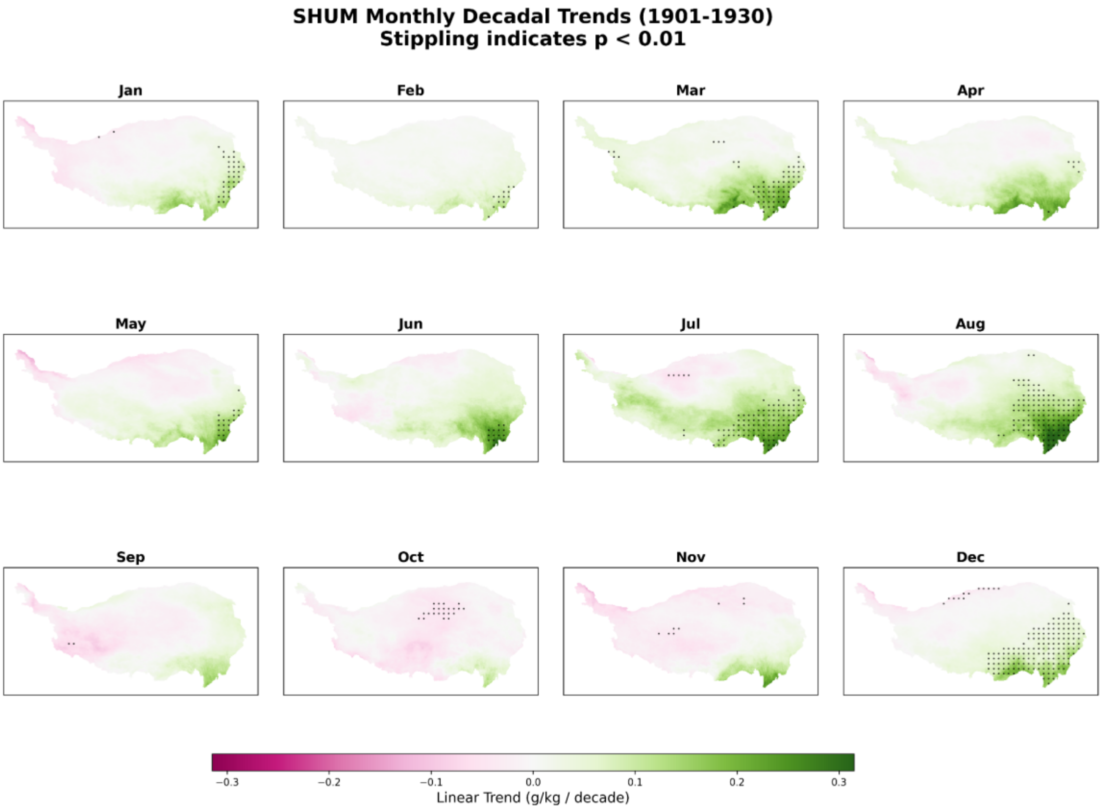

Figure S38. Humidity trends for each calendar month over the Tibetan Plateau during 1901-1930.

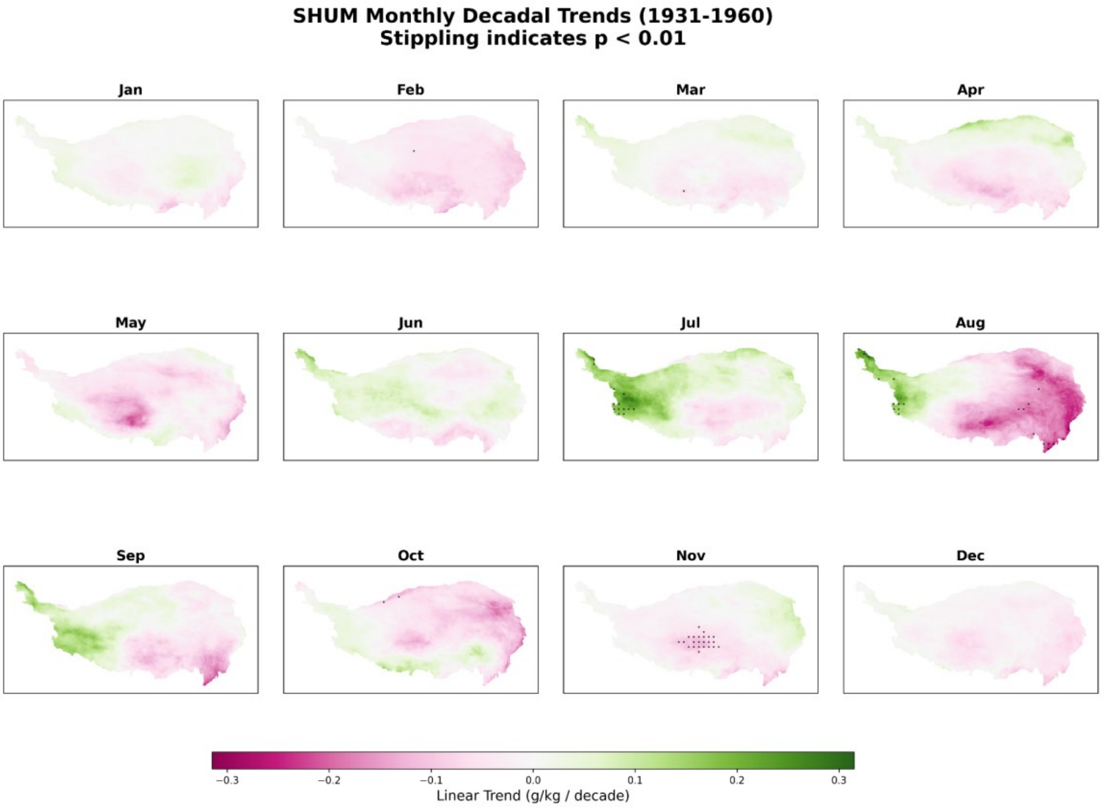

Figure S39. Humidity trends for each calendar month over the Tibetan Plateau during 1931-1960.

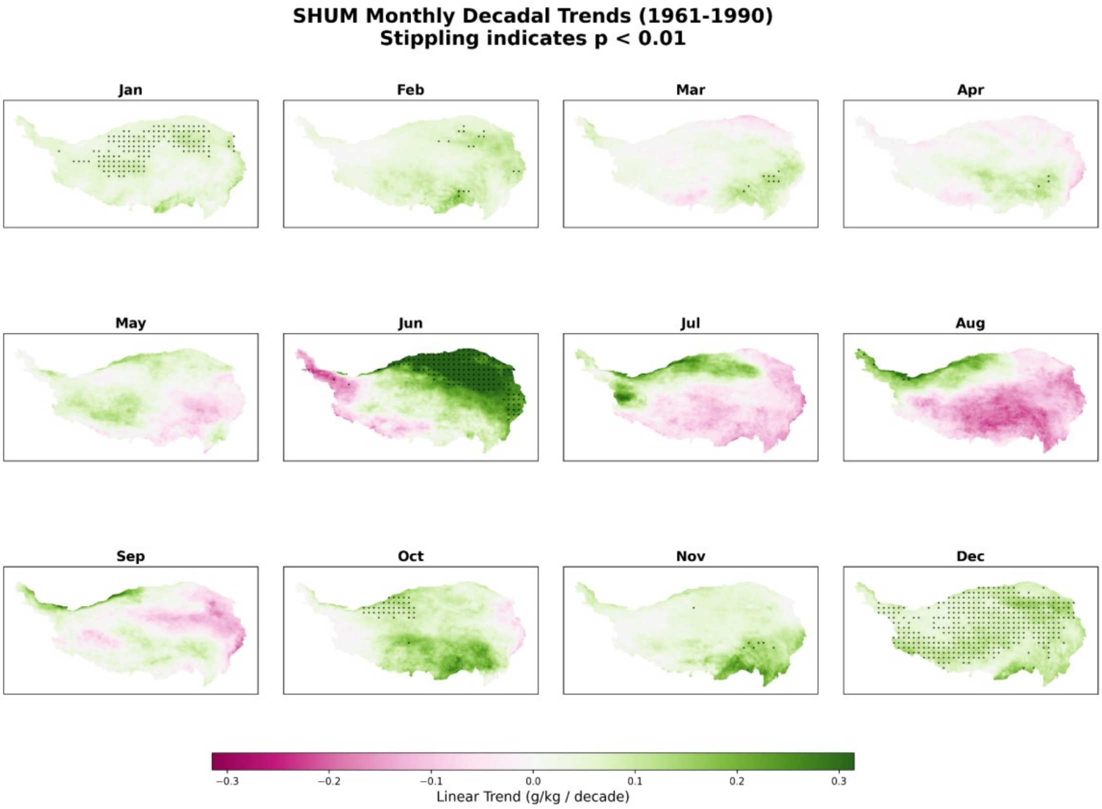

Figure S40. Humidity trends for each calendar month over the Tibetan Plateau during 1961-1990.

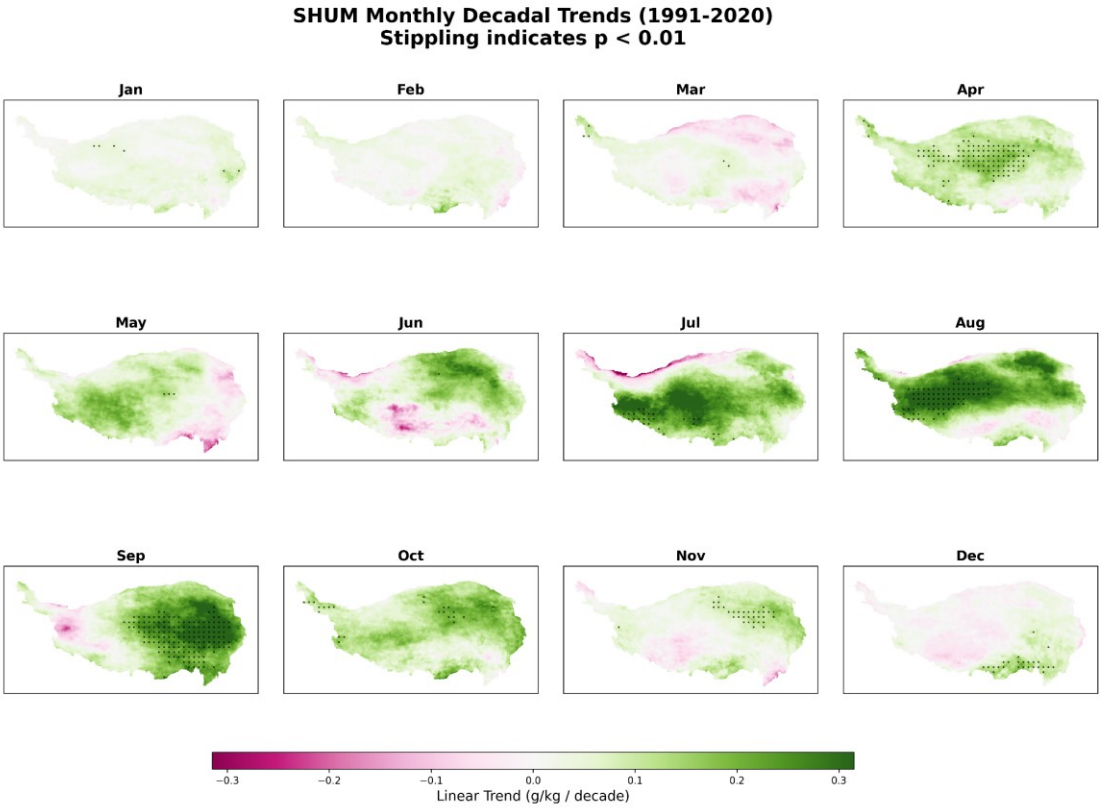

Figure S41. Humidity trends for each calendar month over the Tibetan Plateau during 1991-2020.

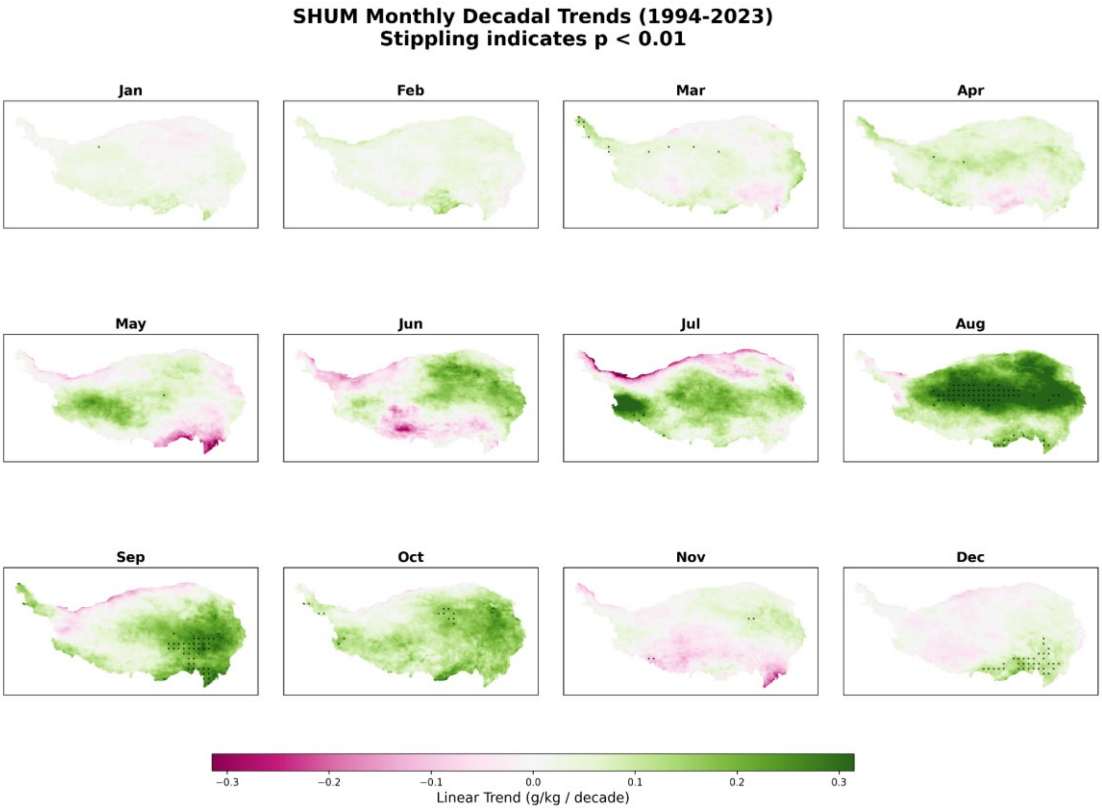

Figure S42. Humidity trends for each calendar month over the Tibetan Plateau during 1994-2023.

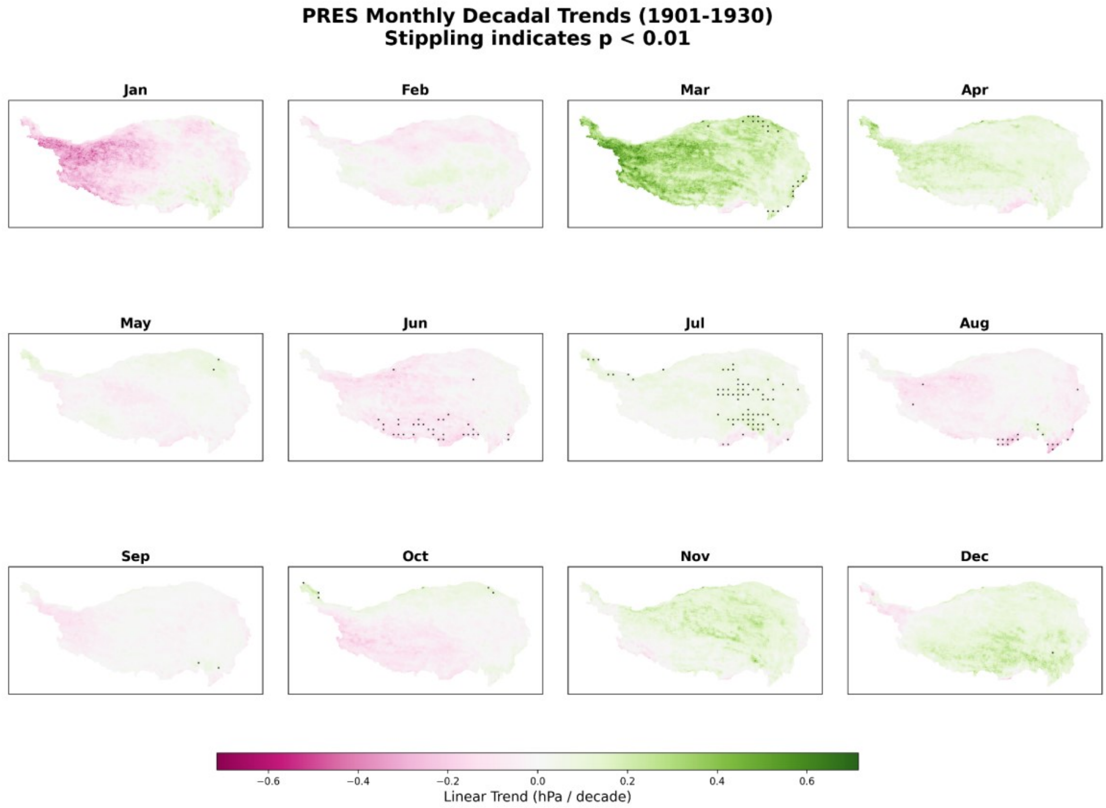

Figure S43. Pressure trends for each calendar month over the Tibetan Plateau during 1901-1930.

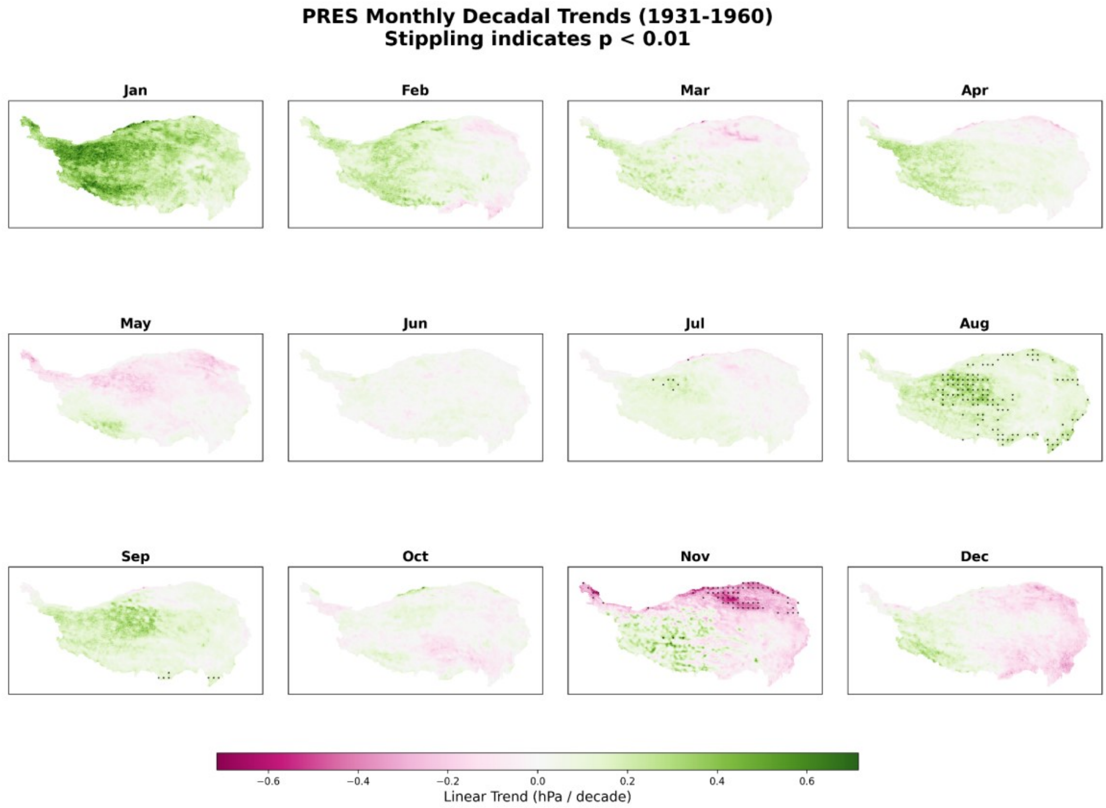

Figure S44. Pressure trends for each calendar month over the Tibetan Plateau during 1931-1960.

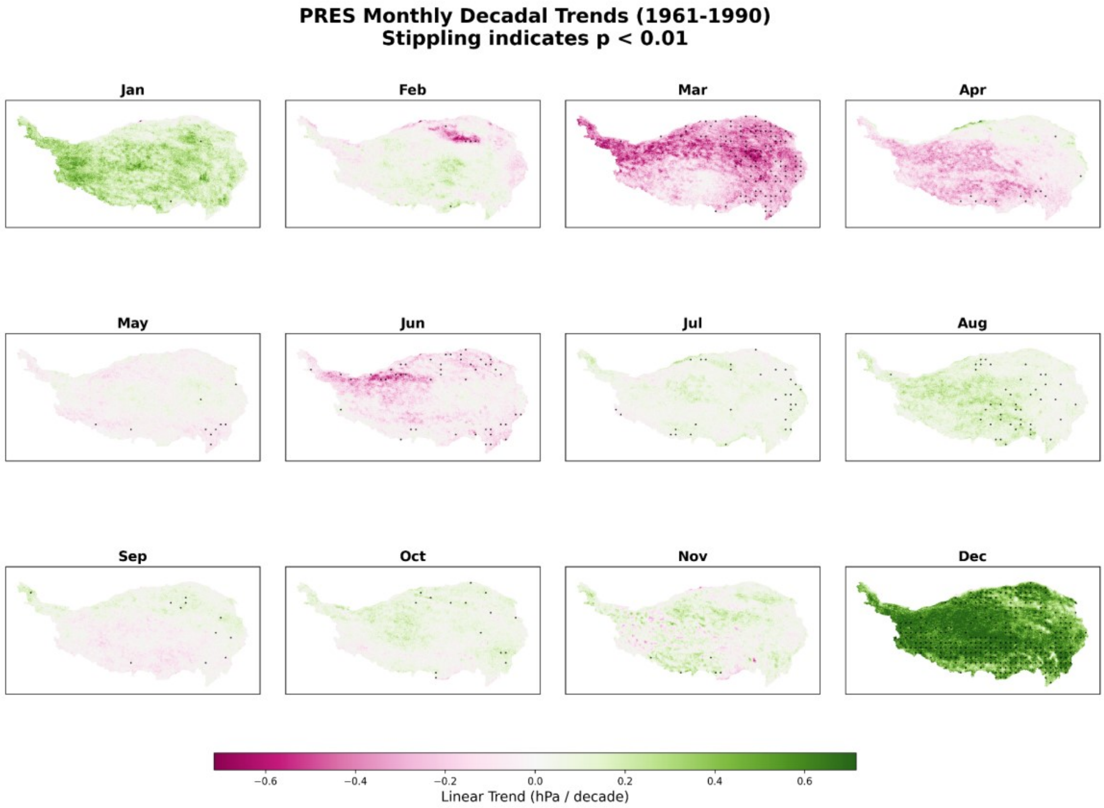

Figure S45. Pressure trends for each calendar month over the Tibetan Plateau during 1961-1990.

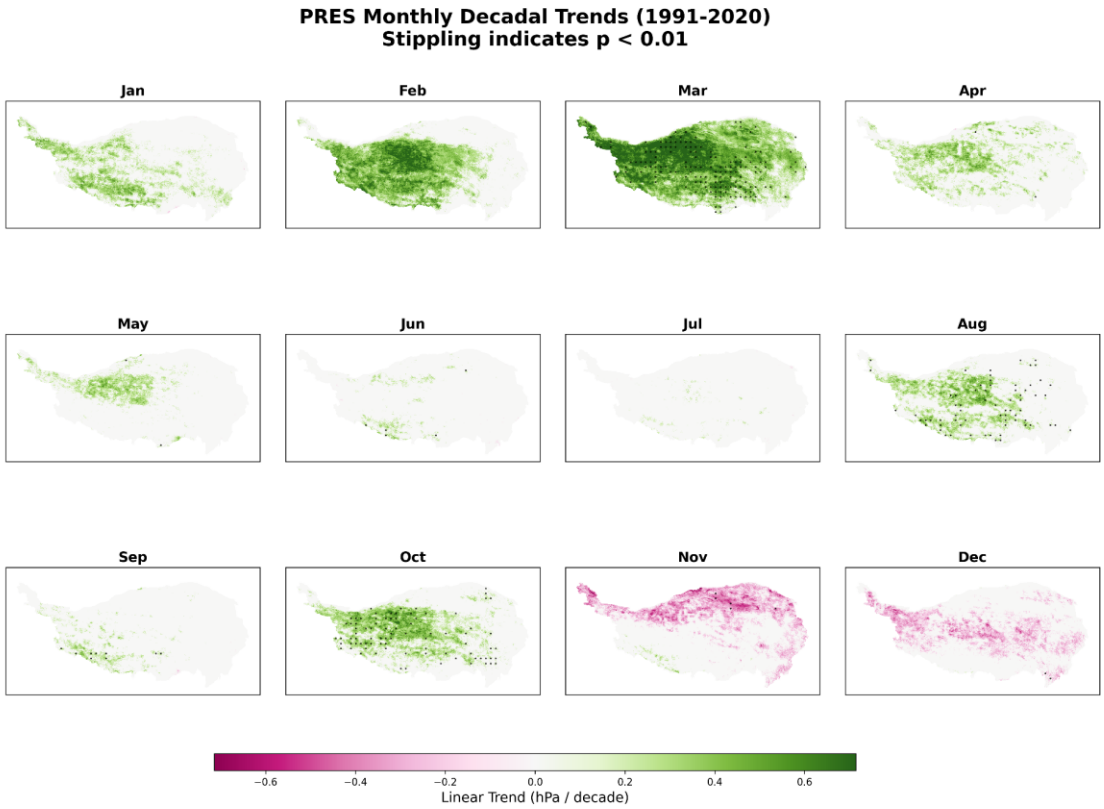

Figure S46. Pressure trends for each calendar month over the Tibetan Plateau during 1991-2020.

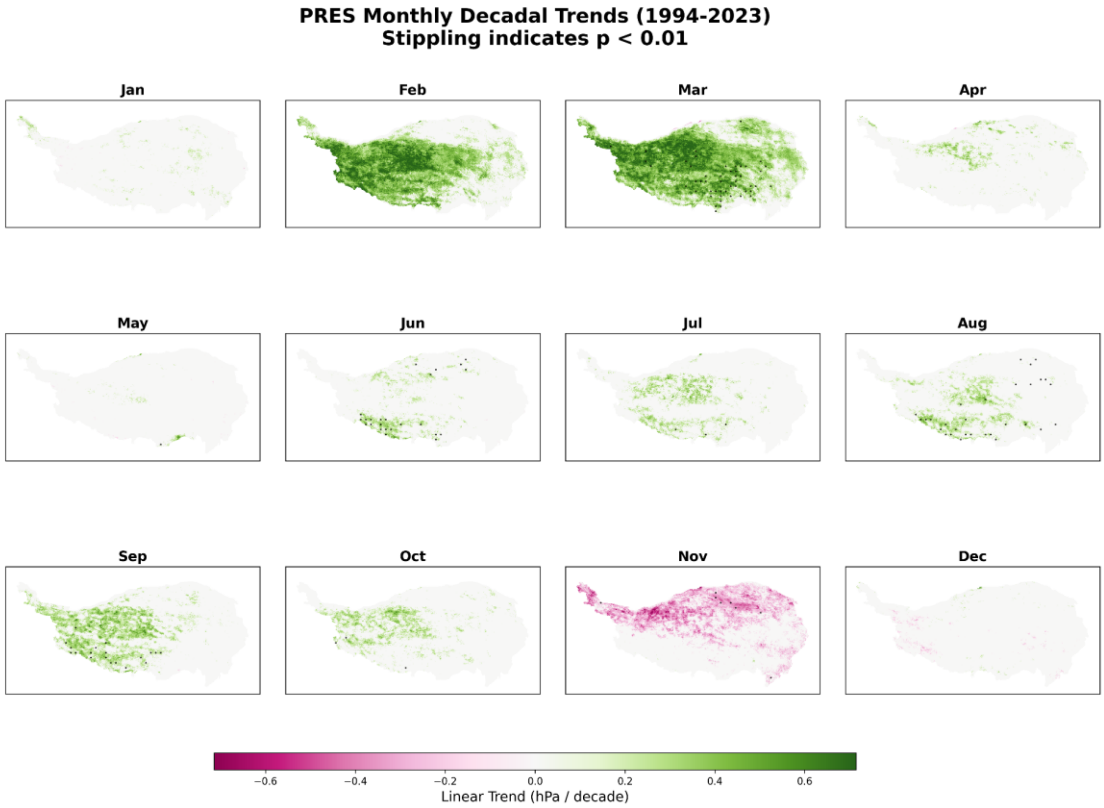

Figure S47. Pressure trends for each calendar month over the Tibetan Plateau during 1994-2023.